Probing the role of synaptic adhesion molecule RTN4RL2 in setting up cochlear connectivity

Nare Karagulyan[1,2,3#], Maja Überegger[4#], Yumeng Qi[5#], Norbert Babai[1,2], Florian Hofer[4], Lejo Johnson Chacko[6], Fangfang Wang[5], Maria Luque[6], Rudolf Glueckert[6], Anneliese Schrott-Fischer[6], Yunfeng Hua[5*], Tobias Moser[1,2,3,7*], Christine Bandtlow[4*]

[1]Institute for Auditory Neuroscience, University Medical Center Göttingen, Göttingen, Germany

[2]Auditory Neuroscience and Synaptic Nanophysiology Group, Max Planck Institute for Multidisciplinary Sciences, Göttingen, Germany

[3]Cluster of Excellence "Multiscale Bioimaging of Excitable Cells", 37075 Göttingen, Germany

[4]Institute of Neurobiochemistry, Biocenter, Medical University of Innsbruck, 6020 Innsbruck, Austria

[5]Shanghai Institute of Precision Medicine, Ninth People's Hospital, Shanghai Jiao Tong University School of Medicine, Shanghai 200125, China

[6]Department of Otorhinolaryngology, Medical University of Innsbruck, 6020 Innsbruck, Austria

[7]Department for Hearing, Speech and Voice Disorders, Medical University of Innsbruck, 6020 Innsbruck, Austria

Running title: Expression and function of RTN4RL2 in the cochlea

[#]equal contribution
*correspondence to
Dr. Christine Bandtlow: christine.bandtlow@i-med.ac.at
Dr. Tobias Moser: tmoser@gwdg.de
Dr. Yunfeng Hua: yunfeng.hua@shsmu.edu.cn

Abstract

Sound encoding depends on the precise and reliable neurotransmission at the afferent synapses between the sensory inner hair cells (IHCs) and spiral ganglion neurons (SGNs). The molecular mechanisms contributing to the formation, as well as interplay between the pre- and postsynaptic components remain largely unclear. Here, we tested the role of the synaptic adhesion molecule and Nogo/RTN4 receptor homolog RTN4RL2 (also referred to as NgR2) in the development and function of afferent IHC-SGN synapses. Upon deletion of RTN4RL2 in mice (RTN4RL2$^{-/-}$), presynaptic IHC active zones showed enlarged synaptic ribbons and a depolarized shift in the activation of $Ca_V1.3$ Ca^{2+} channels. The postsynaptic densities (PSDs) of SGNs were smaller and deficient of GluA2/3 despite maintained Gria2 mRNA expression in SGNs. Next to synaptically engaged PSDs we observed "orphan" PSDs located away from IHCs. They likely belong to a subset of SGN peripheral neurites that do not contact the IHCs in

RTN4RL2$^{-/-}$ cochleae as found by volume electron microscopy reconstruction of SGN neurites. Auditory brainstem responses of RTN4RL2$^{-/-}$ mice showed increased sound thresholds indicating impaired hearing. Together, these findings suggest that RTN4RL2 contributes to the proper formation and function of auditory afferent synapses and is critical for normal hearing.

Introduction

Hearing relies upon the correct formation and maturation of cochlear afferent synapses between postsynaptic type I spiral ganglion neurons (SGNs) and presynaptic inner hair cells (IHCs; reviewed in Johnson et al., 2019; Bulankina and Moser, 2012; Appler and Goodrich, 2011). In mice, SGN neurites extend and reach IHCs at late embryonic stages (E16.5; Koundakjian, Appler, and Goodrich, 2007), whereby early synaptic contacts are established between the two cells at E18 (Michanski et al., 2019). Developmental changes and maturation of afferent synapses continue until the onset of hearing (p12), with further refinement occurring till the fourth postnatal week (Wong et al., 2014; Liberman and Liberman, 2016; Michanski et al., 2019). In mature cochleae, each IHC receives a contact from 5-30 SGNs, while each SGN contacts only one active zone (AZ) of one IHC in the majority of cases (Meyer and Moser, 2010; Hua et al., 2021).

To this date, multiple mechanisms have been implicated in SGN neurite guidance and establishment of IHC innervation by SGNs, including signaling via EphrinA5-EphA4, Neuropilin2/Semaphorin3F, Semaphorin5B/PlexinA1, Semaphorin3A (Defourny et al., 2013; Coate et al., 2015; Jung et al., 2019; Cantu-Guerra et al., 2023). Less is known about the molecules governing the transsynaptic organization at IHC afferent synapses. Similar to the central conventional synapses, synaptic adhesion proteins such as neurexins and neuroligins have been suggested to play a role in pre- and postsynaptic assemblies (Ramirez et al., 2022; Jukic et al., 2024). Furthermore, the $Ca_V1.3$ extracellular auxiliary subunit $Ca_V\alpha_2\delta_2$ was indicated to be important for proper alignment of presynaptic IHC AZs and postsynaptic densities (PSDs) of SGNs (Fell et al., 2015).

Whether reticulon 4 receptors (RTN4Rs) contribute to setting up afferent connectivity in the cochlea remained to be investigated. The RTN4 receptor family consists of 3 homologous proteins RTN4R, RTN4RL1 and RTN4RL2. RTN4Rs are leucine-rich repeat (LRR) and glycosylphosphatidylinositol (GPI) anchored cell surface receptors (Figure 1A). Their

primary role is thought to limit synaptic plasticity and axonal outgrowth as well as to restrict axonal regeneration after injury (reviewed in Mironova and Giger, 2013). While RTN4R and RTN4RL1 are involved in axonal guidance (Vaccaro et al., 2022), RTN4RL2 has been proposed to be important for innervation of the epidermis by dorsal root ganglion neurons (Bäumer et al., 2014). Furthermore, RTN4Rs are suggested to control the number and the development of synapses (Wills et al., 2012) and to play a role in transsynaptic signaling (Wang et al., 2021).

Recent single-cell transcriptomic studies of the cochlea detected the expression of RTN4Rs in SGNs and IHCs (Shrestha et al., 2018; Jean et al., 2023). Here, we investigated the role of RTN4RL2 in the cochlea using previously described RTN4RL2 constitutive knock-out mice (RTN4RL2$^{-/-}$; Wörter et al., 2009). We found RTN4RL2 to be expressed in SGNs and to be required for normal hearing: auditory brainstem responses were impaired upon RTN4RL2 deletion. We discovered both pre- and postsynaptic alterations of IHC-SGN synapses in RTN4RL2$^{-/-}$ mice: presynaptic Ca^{2+} channels of IHCs required stronger depolarization to activate and PSDs seemed deficient of GluA2/3. Additionally, a subset of type I SGN neurites did not contact IHCs but likely still feature “orphan” PSDs.

Results

RTN4RL2 is expressed both in hair cells and spiral ganglion neurons

Recent transcriptomic data had detected RTN4RL2 expression both in hair cells and SGNs (Elkon et al., 2015; Liu et al., 2018; Shrestha et al., 2018; Jean et al., 2023). We verified this by performing RNAscope staining in mid-modiolar sections of the cochlea and detected expression of RTN4RL2 mRNA both in outer and inner hair cells, as well as SGNs (Figure 1B, C). Spiral ganglia of RTN4RL2$^{-/-}$ mice were lacking RTN4RL2-specific mRNA puncta (Figure 1C), demonstrating specific detection of RTN4RL2 expression in hair cells and SGNs. Next, we performed immunostaining and found specific RTN4RL2 immunofluorescence in SGN somata, which was not present in the absence of the primary antibody (Figure 1D, E) or on SGN somata of RTN4RL2$^{-/-}$ mice (data not shown).

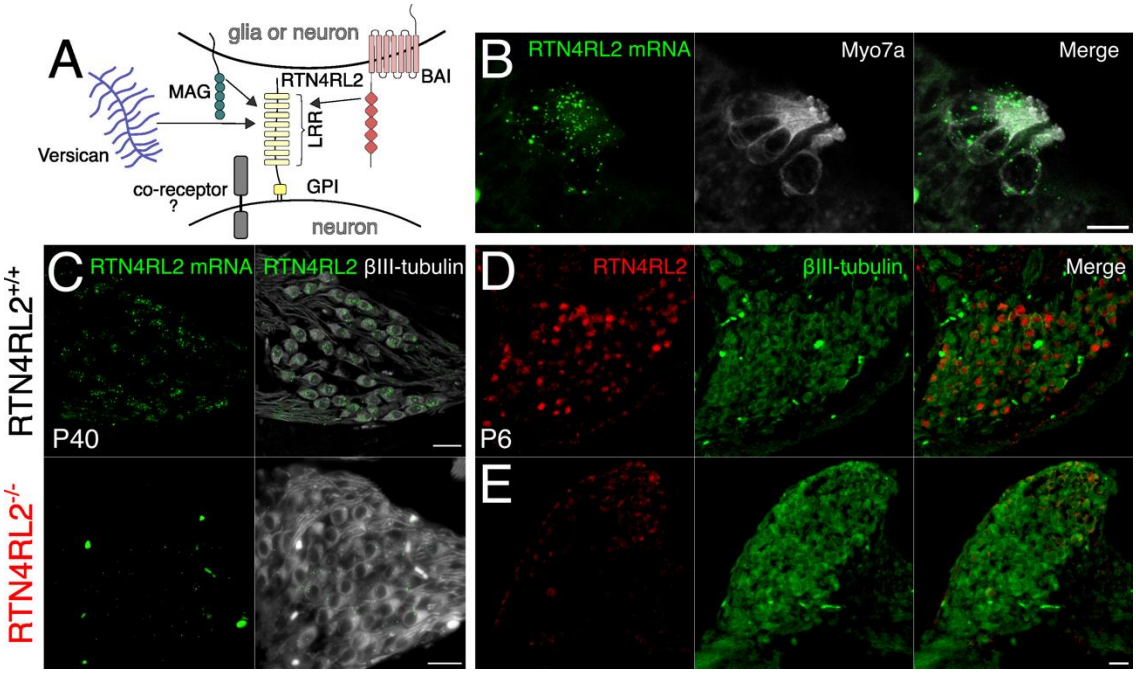

Figure 1. RTN4RL2 mRNA and protein expression in IHCs and SGNs of the mouse cochlea. (**A**) RTN4RL2 is an LRR protein and is anchored to the cell membrane via GPI. In the nervous system RTN4RL2 has been implicated to interact with MAG, versican, BAI. (**B**) Representative images of RNAscope ISH for RTN4RL2 mRNA (green dots) in the hair cell region of p1 wild-type animals. Hair cells are visualized with anti-Myo7a stainings. Scale bar = 10 μm. (**C**) Representative images of RNAscope ISH for RTN4RL2 mRNA (green dots) combined with immunostaining for neuron-specific marker βIII-tubulin (grey) in paraffin sections of p40 RTN4RL2$^{+/+}$ and RTN4RL2$^{-/-}$ spiral ganglion sections. Scale bar = 20 μm. (D) Double immunostaining with anti-RTN4RL2 and βIII-tubulin on cryosections of p6 spiral ganglia. Immunoreactivity of RTN4RL2 (red) was colocalized with βIII-tubulin positive neurons (grey). (E) No specific signal was detected by omitting the primary RTN4RL2 antibody (negative control). Scale bar = 20 μm.

RTN4RL2 is important for the correct development of the auditory afferent synapses

To probe the role of RTN4RL2 in the cochlea, we first studied the numbers of cochlear cells in RTN4RL2$^{-/-}$ mice. We did not observe any change in SGN density or counts of inner and outer hair cells at p15, 1-month- and 2-month-old mice (Figure 2-figure supplement 1). Given that RTN4RL2 has been implicated in synapse formation and development (Wills et al., 2012; Borrie et al., 2014; Wang et al., 2021) we immunolabeled IHC afferent synapses for presynaptic RIBEYE/Ctbp2 and postsynaptic Homer1 in mice at the age of 3 weeks. While we did not detect any change in the number of synaptic ribbons in RTN4RL2$^{-/-}$ IHCs, ribbon volumes were bigger (Figure 2C, D; Figure 2-figure supplement 2). Interestingly, in addition to the Homer1 positive

115 puncta juxtaposing presynaptic ribbons, we observed additional Homer1 patches, which
116 appeared to be away from IHCs, potentially marking “orphan” PSDs (Figure 2A, B). Moreover,
117 the Homer1 puncta juxtaposing IHC AZs were significantly smaller in RTN4RL2$^{-/-}$ mice
118 compared to the control IHCs (Figure 2E). While we found the percentage of presynaptic
119 ribbons juxtaposing Homer1 immunofluorescent puncta to be decreased by approximately
120 7% in RTN4RL2$^{-/-}$ mice (Figure 2F), we cannot exclude that our immunolabeling protocol lacked
121 the sensitivity to detect smaller synaptically engaged PSDs. Out of the four pore-forming
122 AMPA receptor subunits (GluA1-4), mature SGNs express GluA2-4 (Niedzielski and Wenthold,
123 1995; Matsubara et al., 1996). Our immunolabeling of anti-GluA2/3 revealed a severe
124 reduction of GluA2/3 positive puncta in RTN4RL2$^{-/-}$, indicating possible lack or decrease of
125 GluA2/3 (Figure 2-figure supplement 3A, B). Interestingly, the remaining GluA2/3 patches did
126 not properly juxtapose presynaptic ribbons (Figure 2-figure supplement 3C). Despite this, the
127 expression of Gria2 RNA appeared to be maintained in SGNs, as indicated by RNAscope (Figure
128 2-figure supplement 3D). To check if the “orphan” PSDs away from IHCs were possibly
129 erroneously engaged with efferent presynaptic terminals we stained the latter for synapsin,
130 which is lacking from IHCs, but did not observe any obvious juxtaposition between the
131 “orphan” Homer1 and synapsin puncta (Figure 2-figure supplement 4).

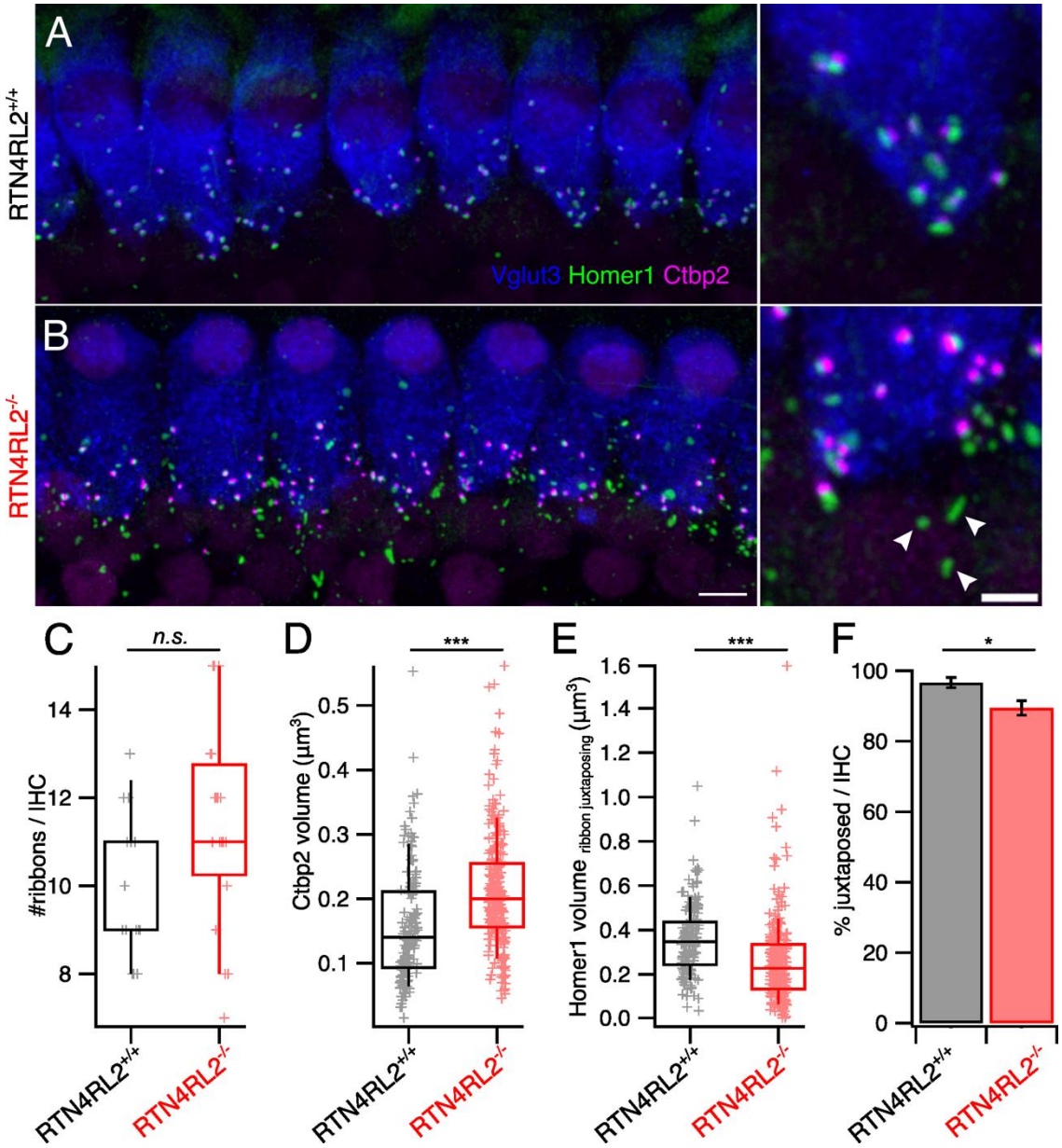

Figure 2. Pre- and postsynaptic changes at IHCs of RTN4RL2$^{-/-}$ mice. (**A, B**) Maximal intensity projections of representative confocal stacks of IHCs from RTN4RL2$^{+/+}$ (A) and RTN4RL2$^{-/-}$ (B) mice immunolabeled against Vglut3, Homer1, and Ctbp2. Scale bar = 5 µm. Images on the right-hand side are zoomed into the synaptic regions. Scale bar = 2 µm. Some of the putative "orphan" PSDs are marked with the white arrowheads. (**C**) Number of Ctbp2 positive puncta is not changed in IHCs of RTN4RL2$^{-/-}$ mice (RTN4RL2$^{+/+}$: 9.9 ± 0.42, SD = 1.62, n = 15, N = 2 vs RTN4RL2$^{-/-}$: 11.4 ± 0.5, SD = 2.25, n = 20, N = 3; p = 0.06, Mann-Whitney-Wilcoxon test). (**D**) Ribbon volumes are enlarged in RTN4RL2$^{-/-}$ IHCs (RTN4RL2$^{+/+}$: 0.16 ± 0.007 µm^3, SD = 0.09 µm^3, n = 165, N = 2 vs RTN4RL2$^{-/-}$: 0.21 ± 0.005 µm^3, SD = 0.09 µm^3, n = 259, N = 3; p < 0.001, Mann-Whitney-Wilcoxon test). (**E**) Homer1 patches which are juxtaposing presynaptic ribbons show decreased volumes in RTN4RL2$^{-/-}$ IHCs (RTN4RL2$^{+/+}$: 0.36 ± 0.01 µm^3, SD = 0.16 µm^3, n = 160, N = 2 vs RTN4RL2$^{-/-}$: 0.26 ± 0.01 µm^3, SD = 0.19 µm^3, n = 249, N = 3; p < 0.001, Mann-Whitney-Wilcoxon test). (**F**) Percentage of Ctbp2 puncta juxtaposing Homer1 is slightly decreased in

146 RTN4RL2$^{-/-}$ mice (RTN4RL2$^{+/+}$: 96.7 ± 1.45 %, SD = 5.44 %, n = 14, N = 2 vs RTN4RL2$^{-/-}$: 89.5 ±
147 2.05 %, SD = 9.18 %, n = 20, N = 3; p = 0.03, Mann-Whitney-Wilcoxon test). Data is presented
148 as mean ± SEM. Box-whisker plots show the median, 25/75 percentiles (box), and 10/90
149 percentiles (whiskers). Individual data points are overlaid.
150

151 ## Additional non-synaptic neurites in the cochlea of RTN4RL2$^{-/-}$ mice

152

153 To further examine the afferent cochlear connectivity, we utilized serial block-face scanning
154 electron microscopy (SBEM) to 3D reconstruct the apical cochlea segments from two
155 RTN4RL2$^{-/-}$ and one littermate RTN4RL2$^{+/+}$ control mice at p36 (Figure 3A). As recently
156 demonstrated (Hua et al., 2021; Lu et al., 2024), the spatial resolution of SBEM allows reliable
157 ribbon synapse identification and neurite reconstruction (Figure 3B and C). In these three
158 datasets, we have traced 133 neural fibers from their postsynaptic ending in the organ Corti
159 towards the modiolus, of which 115 were classified as peripheral neurites of type I SGN based
160 on their radial calibers and extensive myelination after entering the habenula perforata
161 (Figure 3D). We observed a substantial number of neurites that did not engage the IHCs (non-
162 synaptic neurites) in the RTN4RL2$^{-/-}$ organs of Corti (23 out of 83) in contrast to the wild-type
163 control (3 out of 32, Figure 3E). Although most non-synaptic neurites were found in the inner
164 spiral bundle, they failed to reach IHC basal lateral poles to form contacts (17 out of 23 in
165 RTN4RL2$^{-/-}$ animals). This result might provide a plausible explanation for the "orphan"
166 Homer1 puncta shown by immunohistochemistry in RTN4RL2$^{-/-}$ organs of Corti. Note that the
167 presence of non-synaptic neurites in the RTN4RL2$^{-/-}$ animal was not associated with a
168 profound reduction in ribbon synapses (Figure 2C, Figure 2-figure supplement 2B, Figure 3-
169 figure supplement 1A), suggesting a different scenario than deafferentation due to excitotoxic
170 synaptopathy as recently reported (Moverman et al., 2023). Nevertheless, nearly all traced
171 radial fibers were found predominantly unbranched in both the RTN4RL2$^{-/-}$ (97%) and the
172 wild-type control mice (94%; Figure 3F).

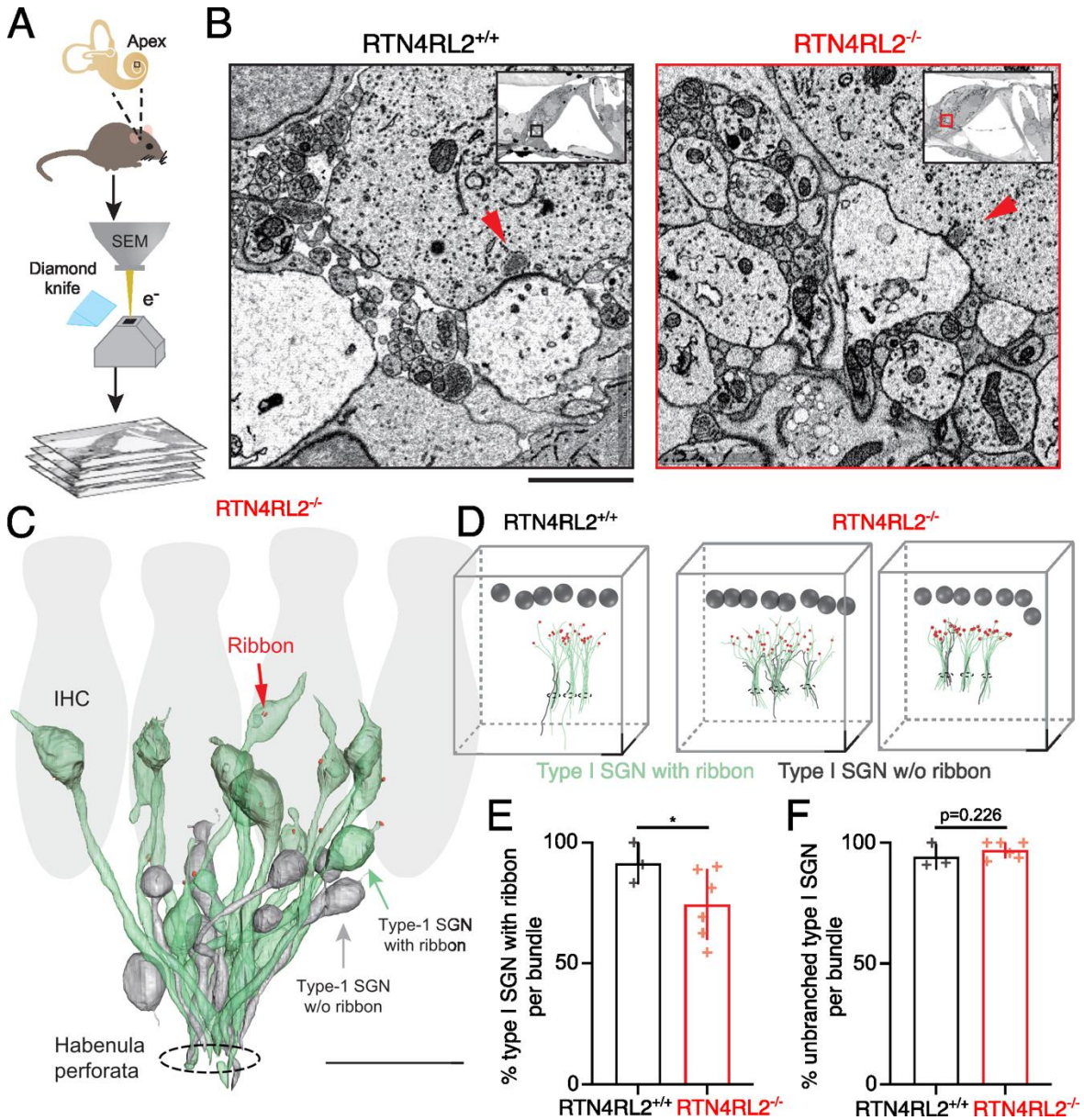

Figure 3. Additional non-synaptically engaged SGN neurites in the cochlea of RTN4RL2$^{-/-}$ mice. (**A**) Workflow of SBEM imaging at the mouse apical cochlear region. (**B**) Example images of neurites beneath IHCs from the RTN4RL2$^{+/+}$ (left) and RTN4RL2$^{-/-}$ (right) mice. Synaptic ribbons are indicated with red arrows. The regions of interest were magnified from single sections of SBEM datasets (insets). Scale bar = 2 µm. (**C**) 3D rendering of afferent fiber reconstruction with ribbons (red), showing both synaptic (green, type I SGN with ribbon) and non-synaptic (grey, type I SGN without ribbon) populations in the RTN4RL2$^{-/-}$ mouse. Scale bar = 10 µm. (**D**) Display of classified radial fibers in the RTN4RL2$^{+/+}$ (left) and RTN4RL2$^{-/-}$ (middle and left) animals. All fibers were traced from the habenula perforata (cycles) before classification to avoid bias to terminal types. Scale bar 10 µm. (**E**) Percentage of radial fibers with ribbon per bundle (RTN4RL2$^{+/+}$: 91.41 ± 8.35 %, n = 3 bundles, N = 1 vs RTN4RL2$^{-/-}$: 74.40 ± 14.58%, n = 6 bundles, N = 2; p = 0.032, unpaired t-test). (**F**) Percentage of unbranched radial fibers per bundle (RTN4RL2$^{+/+}$: 94.19 ± 5.04 %, n = 3 bundles, N = 1 vs RTN4RL2$^{-/-}$: 96.98 ± 3.49 %, n = 6 bundles, N = 2; p = 0.226, unpaired t-test).

188 ## Deletion of RTN4RL2 results in depolarized shift of the Ca^{2+} channel activation in IHCs
189

190 Next, we tested for potential effects of RTN4RL2 deletion on the presynaptic IHC function. We
191 performed whole-cell patch-clamp recordings from IHCs of p21-29 RTN4RL2$^{+/+}$ and RTN4RL2^{-}
192 $^{/-}$ mice. First, we recorded voltage-gated Ca^{2+} currents by applying step depolarizations with 5
193 mV increment in ruptured patch-clamp configuration (Figure 4A, see Materials and Methods).
194 We did not observe any change in the maximal Ca^{2+} current amplitude (Figure 4B, C), yet
195 noticed small (~ +3 mV) but consistent and statistically significant depolarized shift of the
196 voltage of half-maximal Ca^{2+} channel activation (V_{half}; Figure 4D, E). The voltage sensitivity of
197 the channels was not changed in RTN4RL2$^{-/-}$ IHCs (Figure 4F). Next, we probed Ca^{2+} influx
198 triggered exocytosis from IHCs by applying depolarizations of varying durations to voltages
199 saturating Ca^{2+} influx in IHCs of both genotypes (-17 mV) and recording exocytic membrane
200 capacitance changes (ΔC_m) in the perforated patch-clamp configuration (Figure 4G). Both fast
201 (up to 20 ms depolarization) and sustained components of exocytosis remained intact in the
202 mutant, indicating unaffected readily releasable pool and replenishment of the vesicles in
203 RTN4RL2$^{-/-}$ IHCs (Figure 4H).

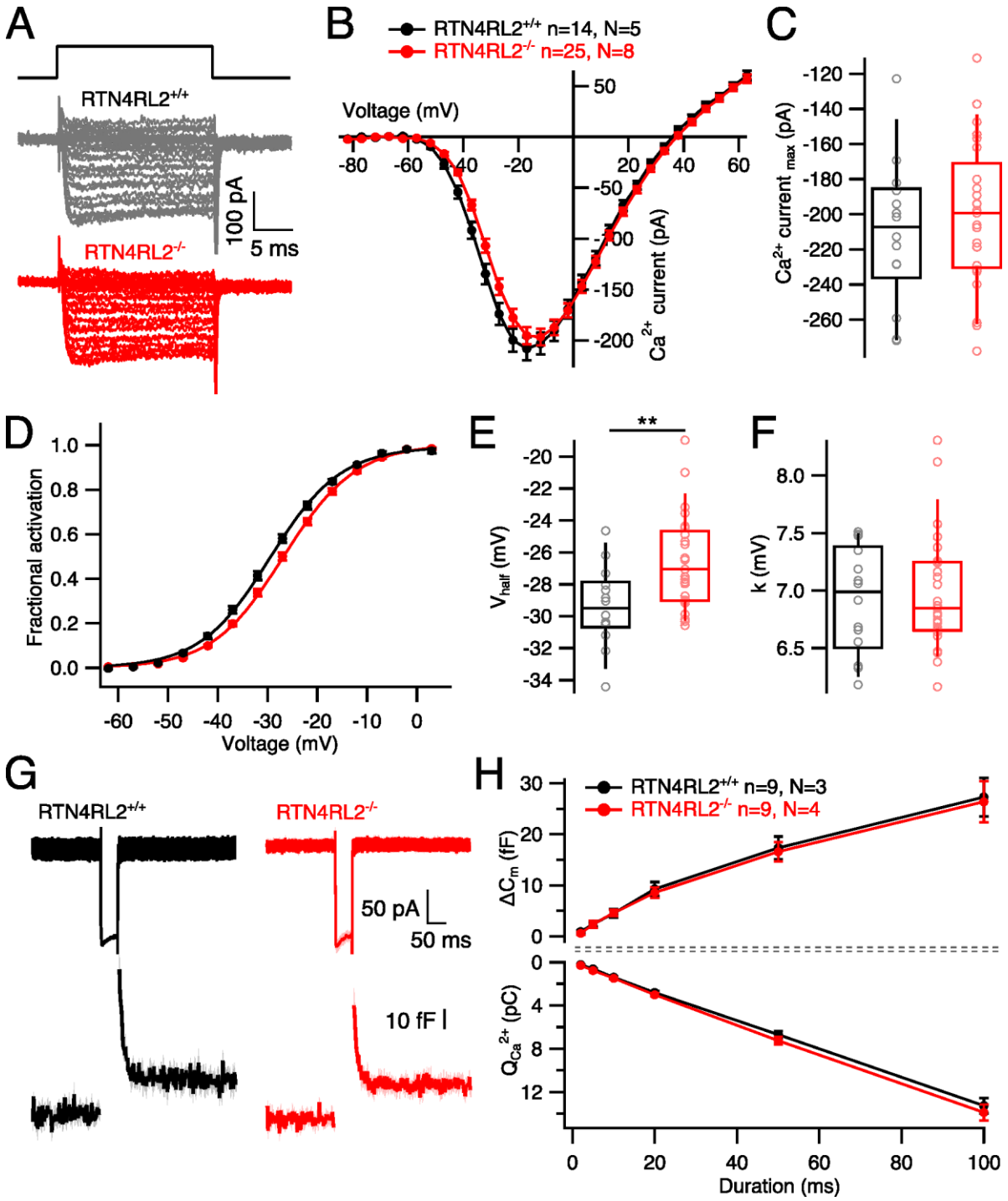

Figure 4. Shifted operation range of Ca^{2+} channels but intact exocytosis in IHCs of RTN4RL2$^{-/-}$ mice. (**A**) Representative current traces from IHCs of RTN4RL2$^{+/+}$ (top, black) and RTN4RL2$^{+/+}$ (bottom, red) evoked by step depolarizations. (**B**) Average Ca^{2+} current-voltage relationships (IV curves) in RTN4RL2$^{+/+}$ and RTN4RL2$^{-/-}$ IHCs. (**C**) Maximal Ca^{2+} current amplitude is not changed in RTN4RL2$^{-/-}$ IHCs (RTN4RL2$^{+/+}$: 210 ± 10.9 pA, SD = 40.9 pA, n = 14, N = 5 vs RTN4RL2$^{-/-}$: -200 ± 8.19 pA, SD = 40.9 pA, n = 25, N = 8; p = 0.47, Student's t-test). (**D**) Fractional activation curves of Ca^{2+} channels calculated from IVs show depolarized shift in channel activation in RTN4RL2$^{-/-}$ IHCs. (**E**) Voltage of half maximal activation obtained from Boltzmann fit of the curves from (D) is more positive in RTN4RL2$^{-/-}$ IHCs (RTN4RL2$^{+/+}$: -29.4 ± 0.66 mV, SD

= 2.48 mV, n = 14, N = 5 vs RTN4RL2$^{-/-}$: -26.6 ± 0.59 mV, SD = 2.94 mV, n = 25, N = 8; p = 0.004, Student's t-test). (**F**) Voltage sensitivity (k) is not changed in RTN4RL2$^{-/-}$ IHCs (RTN4RL2$^{+/+}$: 6.92 ± 0.12 mV, SD = 0.46 mV, n = 14, N = 5 vs RTN4RL2$^{-/-}$: 6.98 ± 0.1 mV, SD = 0.51 mV, n = 25, N = 8; p = 0.93, Mann-Whitney-Wilcoxon test). (**G**) Average current traces evoked by 50 ms depolarization to -17mV (top row) and resulting capacitance response (bottom row) from RTN4RL2$^{+/+}$ (left, black) and RTN4RL2$^{+/+}$ (right, red) IHCs. Shaded areas represent ± SEM. (**H**) Exocytic capacitance change (ΔC_m, top) and corresponding Ca^{2+} charge ($Q_{Ca}{}^{2+}$, bottom) evoked by depolarizations (to -17 mV) of various durations (2, 5, 10, 20, 50, 100 ms). Box-whisker plots show the median, 25/75 percentiles (box) and 10/90 percentiles (whiskers). Individual data points are overlaid.

We then turned to study single AZ function by combining whole cell ruptured patch-clamp combined with spinning disc confocal imaging of presynaptic Ca^{2+} influx, as described previously (Ohn et al., 2016). TAMRA conjugated Ctbp2 binding dimeric peptide and the low affinity Ca^{2+} indicator Fluo4-FF (k_D: 10 µM) were loaded into the cell via the patch pipette and Ca^{2+} influx at single AZs was visualized in the form of hotspots by applying voltage ramp depolarizations to the IHCs and simultaneously imaging Fluo4-FF fluorescence near labeled ribbons (Figure 5A, see Materials and methods). Maximal Ca^{2+} influx at single AZs tended to be higher in IHCs of RTN4RL2$^{-/-}$ mice but the difference did not reach statistical significance (Figure 5B, B^{i}). The V_{half} of Ca^{2+} channel clusters at single AZs showed depolarized shift (~ +5 mV), which was statistically significant despite the large variability of V_{half} across different AZs (Figure 5C, C^{i}). Furthermore, we did not observe any mismatch in Ctbp2 positive puncta and evoked Ca^{2+} hotspots, indicating the correct localization of Ca^{2+} channels at the AZs. We verified this by performing immunostainings of $Ca_v1.3$, Ctbp2 and Bassoon and did not detect any apparent misalignment of these protein clusters (Figure 5D). In summary, deletion of RTN4RL2 causes a depolarized shift of the activation of presynaptic Ca^{2+} influx in IHCs as demonstrated at the single AZ and whole cell levels. This is expected to elevate the sound pressure levels required to reach a comparable activity of synaptic transmission for sound encoding and predicts elevated auditory thresholds which we tested by recordings of auditory brainstem responses.

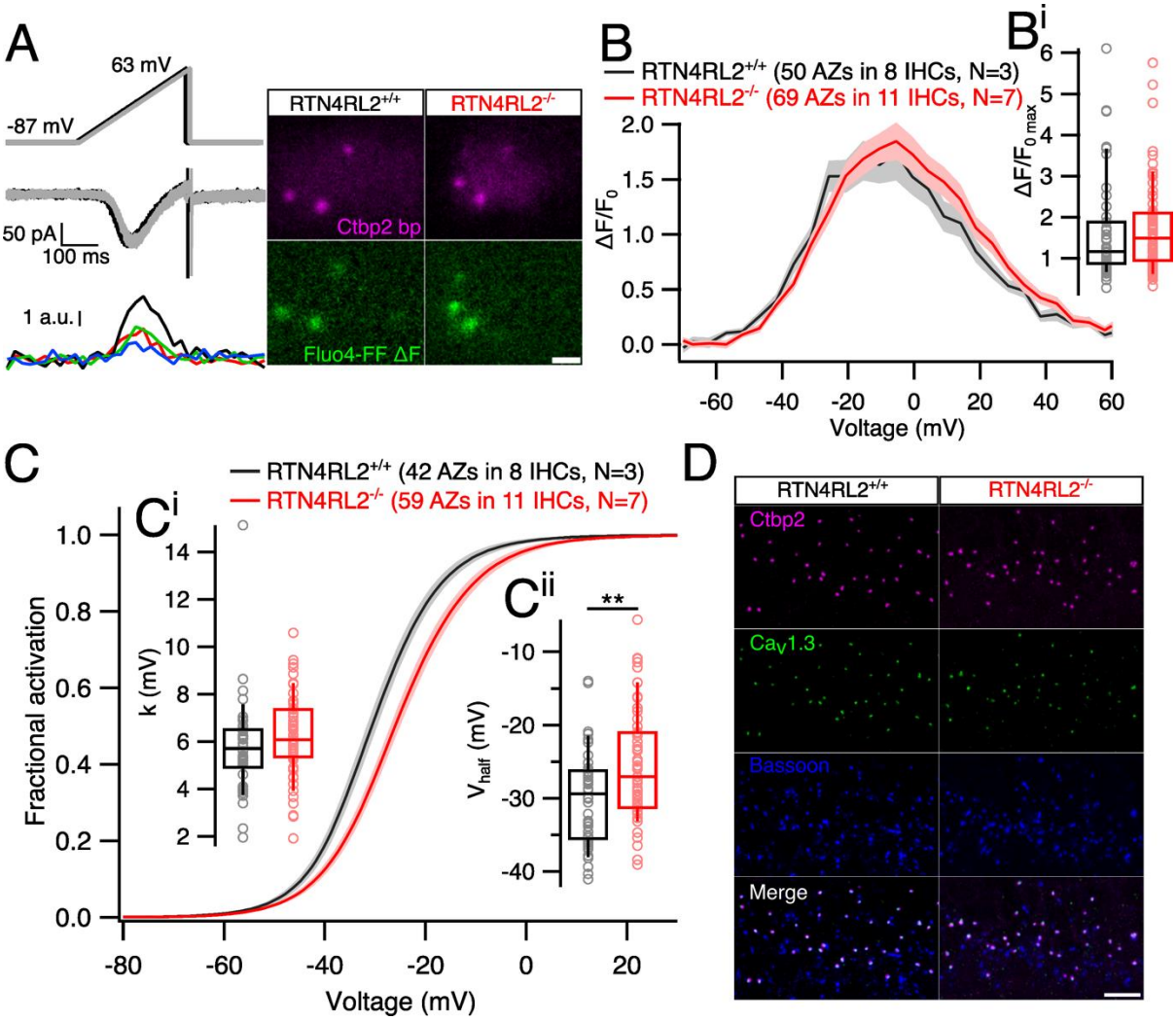

Figure 5. Depolarized shift of Ca^{2+} channel activation at single AZs but intact presynaptic organization in RTN4RL2$^{-/-}$ IHCs. (**A**) Voltage ramp stimulation protocols (top), evoked whole cell currents (middle) and the presynaptic hotspots of Fluo4-FF fluorescence (bottom) of a representative IHC recording. Black and grey colors represent the two stimulations, one being 5 ms shifted over the other. Images on the right show single image planes of representative RTN4RL2$^{+/+}$ (left) and RTN4RL2$^{-/-}$ (right) IHCs filled with TAMRA conjugated Ctbp2 binding peptide (Ctbp2 bp) and Fluo4-FF Ca^{2+} dye. Ca^{2+} hotspots are visualized by subtracting the average of baseline planes from the average of 5 planes during stimulation. Scale bar = 2 µm (**B**) Average fluorescence-voltage relationships of Ca^{2+} influx at single AZ from RTN4RL2$^{+/+}$ and RTN4RL2$^{-/-}$ IHCs show no difference in the maximal Ca^{2+} amplitude (**B^{i}**; RTN4RL2$^{+/+}$: 1.6 ± 0.17, SD = 1.2, n = 50 AZs vs RTN4RL2$^{-/-}$: 1.7 ± 0.13 pA, SD = 1.09, n = 69 AZs; p = 0.24, Mann-Whitney-Wilcoxon test). Shaded areas represent ± SEM. (**C**) Average fractional activation curves of Ca^{2+} channels at single AZs relationships of single AZ show intact voltage sensitivity (**C^{i}**; RTN4RL2$^{+/+}$: 5.79 ± 0.32 mV, SD = 2.04 mV, n = 42 AZs vs RTN4RL2$^{-/-}$: 6.25 ± 0.22 mV, SD = 1.7 mV, n = 59 AZs; p = 0.06, Mann-Whitney-Wilcoxon test) but depolarized shift of V_{half} (**C^{ii}**; RTN4RL2$^{+/+}$: -30 ± 1 mV, SD = 6.5 mV, n = 42 AZs vs RTN4RL2$^{-/-}$: -25.5 ± 0.98 mV, SD = 7.49 mV, n = 59 AZs; p = 0.002, Student's t-test) in RTN4RL2$^{-/-}$ IHCs. Shaded areas represent ± SEM. (**D**) Representative immunolabelings of presynaptic proteins show no apparent mislocalization in RTN4RL2$^{-/-}$ IHCs. Scale bar = 5 µm. Box-whisker plots show the median, 25/75 percentiles (box) and 10/90 percentiles (whiskers). Individual data points are overlaid.

RTN4RL2 is essential for normal hearing

In order to evaluate auditory systems function in RTN4RL2$^{-/-}$ mice, we recorded auditory brainstem responses (ABRs) at the age of 2-4 months. ABRs were elicited in response to 4, 8, 16, 32 kHz tone bursts and click stimuli of increasing sound pressure levels. We determined the sound thresholds by identifying the lowest sound pressure level which resulted in detectable ABR waveform. We found ABR thresholds to be significantly increased by around 30-45 dB across all the tested frequencies and in response to the click stimulations in RTN4RL2$^{-/-}$ mice compared to the wild-type controls (Figure 6). RTN4RL2$^{+/-}$ mice showed an intermediate phenotype between the RTN4RL2$^{-/-}$ and RTN4RL2$^{+/+}$ mice with a lower yet significant increase of ABR thresholds of approximately 10-15 dB at 4, 16 and 32 kHz frequencies.

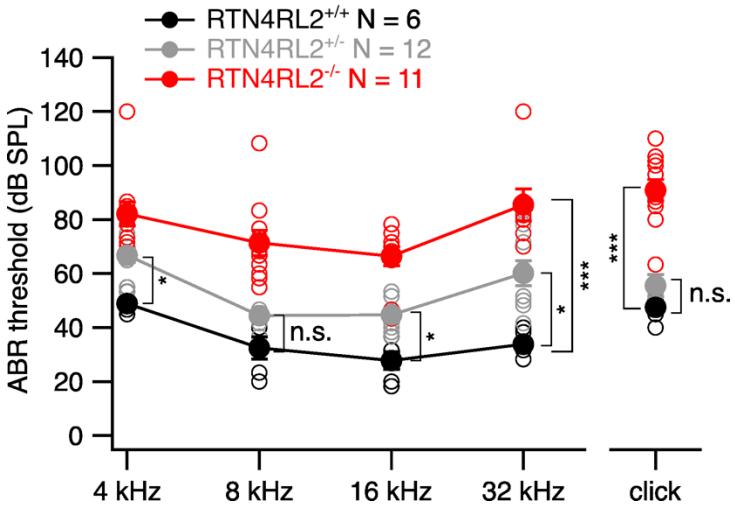

Figure 6. Elevated acoustic thresholds in RTN4RL2$^{-/-}$ mice. ABR thresholds were measured in response to 4, 8, 16, 32 kHz tone bursts and click stimuli. ABR thresholds of individual animals are shown in open circles on top of the mean ± SEM. Statistical significances are reported as *p < 0.05, ***p < 0.001, Kruskal-Wallis followed by Dunn's multiple comparison test.

Discussion

In this study, we investigated the role of the Nogo/RTN4 receptor homolog RTN4RL2 in the cochlea. Consistent with the previous reports, we detected RTN4RL2 expression in IHCs and SGNs. Upon RTN4RL2 deletion, we observed alterations of the IHC-SGN synapses (Figure 7). Presynaptically, Ca^{2+} channel activation was shifted towards depolarized voltages and ribbon size was enlarged. IHC exocytosis was unaltered when probed at saturating depolarizations. At the postsynaptic side, PSDs juxtaposing presynaptic ribbons were smaller compared to the

291 controls and seemed to be deficient of GluA2/3, despite the expression of Gria2 mRNA in
292 RTN4RL2$^{-/-}$ SGNs. Additionally, we observed PSDs which resided further from the IHC
293 membrane and did not juxtapose the presynaptic AZs in RTN4RL2$^{-/-}$ mice. These PSDs
294 potentially belong to the type I SGN neurites that ended in the inner spiral bundle without
295 contacting the IHCs, as observed in SBEM reconstructions of RTN4RL2$^{-/-}$ SGNs. Finally, ABR
296 thresholds were elevated in RTN4RL2$^{-/-}$ mice indicating that RTN4RL2 is required for normal
297 hearing.
298

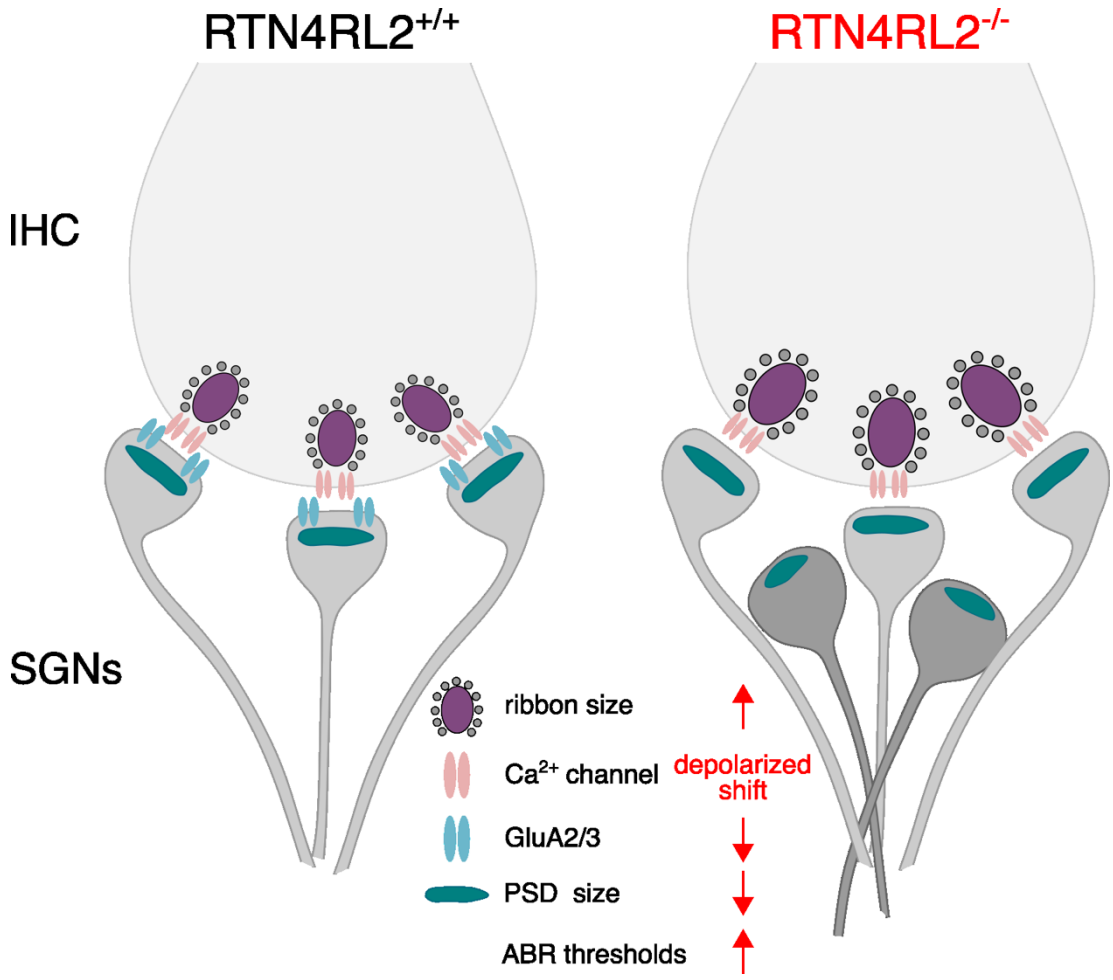

299

300 **Figure 7. Schematic illustration of the key structural and functional changes in the auditory**
301 **periphery of RTN4RL2$^{-/-}$ mice.** RTN4RL2$^{-/-}$ mice display enlarged synaptic ribbons and
302 depolarized shift in the activation of presynaptic Ca^{2+} channels in IHCs, as well as reduced size
303 of PSDs juxtaposing presynaptic ribbons. RTN4RL2 deficiency further results in a subset of
304 type I SGN neurites that reach the inner spiral bundle but do not engage the IHCs.
305

306 RTN4 receptors have been implicated as presynaptic adhesion molecules based on their
307 transsynaptic interactions with postsynaptically enriched brain-specific angiotensin inhibitor

308 (BAI) adhesion GPCRs (Stephenson et al., 2013; Wang et al., 2021). Despite this, at least RTN4R
309 has been proposed to function postsynaptically, given that its knockdown leads primarily to
310 postsynaptic changes (Wills et al., 2012). The interpretation of RTN4R function and localization
311 is further complicated by their enrichment in both pre- and postsynaptic terminals (Wang et
312 al., 2002b). Similarly, we observed RTN4RL2 expression in both IHCs and SGNs. Interestingly,
313 a recent study described a hearing impairment in BAI1 deficient mice and suggested that
314 postsynaptically functioning BAI1 is important for correct localization of AMPA receptor
315 subunits in spiral ganglion neurons based on the absence or decrease of different AMPA
316 receptor subunits at the SGN postsynapses in BAI1 deficient mice (Carlton et al., 2024).
317 Similarly, our data from RTN4RL2$^{-/-}$ mice show the absense of GluA2/3 positive puncta
318 juxtaposing presynaptic AZs. Along with the evidence for transsynaptic interaction between
319 RTN4Rs and BAIs (Wang et al., 2021), this raises the possibility that the GluA2/3 AMPA
320 receptor subunit localization to SGN PSDs requires the interaction of presynaptic RTN4RL2 and
321 postsynaptic BAI1. Likewise, the changes of presynaptic Ca^{2+} channel properties and ribbons
322 in IHCs could result from direct presynaptic action of RTN4RL2. However, further experiments,
323 e.g. in mutants with SGN-specific RTN4RL2 deletion should evaluate a potential direct
324 postsynaptic role of RTN4RL2 including a possible transsynaptic signaling to IHC AZs.
325 Presynaptic changes upon postsynaptic manipulation have been reported previously. For
326 instance, the deletion of postsynaptically expressed Pou4f1 transcription factor resulted in
327 hyperpolarized shift of IHC Ca^{2+} channels, as well as in changes of the presynaptic
328 heterogeneity of IHC AZs (Sherrill et al., 2019). Similarly, presynaptic ribbon sizes were altered
329 in IHCs of mice, which exhibited conditional deletion of Runx1 transcription factor from SGNs
330 (Shrestha et al., 2023).

331 We did not detect RTN4RL2 near the synaptic regions but cannot exclude transient
332 synaptic localization of RTN4RL2 during development. Indeed, localization of RTN4Rs has been
333 shown to be dynamically regulated across different phases of IPSC-derived neuron
334 development (Wang et al., 2021). We propose that the afferent synaptic changes contribute
335 to the severe hearing impairment in RTN4RL2$^{-/-}$ mice. The phenotype of increased ABR
336 thresholds could partially be explained by the depolarized activation of Ca^{2+} channels in IHCs.
337 As it has been shown, the apparent Ca^{2+} dependence of glutamate release from IHCs on
338 average follows a near linear relationship (Wong et al., 2014; Özçete and Moser, 2021; Jaime
339 Tobón and Moser, 2023b, 2023a). Therefore, due to the depolarized shift of the Ca^{2+} channel

340 activation, the glutamate release from IHCs and subsequent spike generation in SGNs would
341 require stronger stimuli. Likewise, depolarized activation of Ca^{2+} channels has been associated
342 with the higher firing thresholds and low spontaneous rates in SGNs of Ribeye knock-out mice,
343 albeit less severe hearing phenotype was observed in those mice (Jean et al., 2018).
344 In addition or alternatively, the increase in auditory thresholds could be caused by the
345 deficiency of GluA2/3 AMPA receptors of the SGN postsynapses in RTN4RL2$^{-/-}$ mice. We cannot
346 exclude that the lack of GluA2/3 subunits can be compensated by the overexpression of GluA4
347 subunit, which was also recently shown in GluA3 KO mice (Rutherford et al., 2023). Given the
348 observed synaptic changes, it seems less likely that the hearing impairment would have
349 resulted from the intrinsic changes of SGN firing. Further experiments, where SGNs would be
350 stimulated directly via *ex vivo* patch-clamp or optogenetically could help to probe for
351 functional deficits in SGN of RTN4RL2$^{-/-}$ mice. Another interesting observation was the
352 additional PSDs not juxtaposing presynaptic ribbons that were detected around IHCs of
353 RTN4RL2$^{-/-}$ mice. These "orphan" PSDs seem not to be part of the efferent synapses formed
354 between LOC/MOCs and SGNs as we verified by simultaneous anti-Homer1 and anti-synapsin
355 immunolabelings. To check the SGN connectivity we performed SBEM in RTN4RL2$^{+/+}$ and
356 RTN4RL2$^{-/-}$ cochlear samples and observed a high percentage of non-synaptic SGN neurites in
357 the reconstructed neurons of inner spiral bundles in RTN4RL2$^{-/-}$ samples. A sizable subset of
358 the non-synaptic SGN boutons did not make a contact with IHCs, potentially housing the
359 "orphan" PSDs observed around the IHCs in our immunolabeled samples. How exactly those
360 non-synaptic neurites appear remains to be investigated. SGN neurite retraction from IHCs
361 has been demonstrated in noise-exposed animals, followed by the degeneration of the SGN
362 somata and axons (Kujawa and Liberman, 2009, 2015; Moverman et al., 2023). This process
363 however results in up to 50% degeneration of the ribbon synapses. Interestingly, in RTN4RL2^{-}
364 $^{/-}$ mice the number of the ribbon synapses as well as the density of the SGN somata was largely
365 intact. This indicates that the non-synaptic neurites do not result from synaptic loss as found
366 in hereditary or acquired synaptopathy (Roux et al., 2006; Ruel et al., 2008; Seal et al., 2008;
367 Kujawa and Liberman, 2009). Although it is plausible that the non-synaptic SGN neurites may
368 fail to reach the IHCs during initial development, it is unlikely that this would selectively impact
369 only a subset of neurons and still allow the Homer1-positive patches to develop in the absence
370 of presynaptic components. Alternatively, it is known that major synaptic pruning takes place
371 in developing SGNs, whereby up to 50% of the synapses are lost between the IHCs and the

372 SGNs (Defourny et al., 2013; Coate et al., 2019), suggesting, that the non-synaptic SGN
373 neurites of RTN4RL2$^{-/-}$ mice could be a result of failed pruning of SGNs during the
374 development. Yet how this would then comply with normal synapse and SGN counts remains
375 to be elucidated. Future studies will be required to quantify the type I SGN projections of
376 RTN4RL2$^{-/-}$ mice during development and to trace their neurites from the soma to the organ
377 of Corti to probe for potential branching in the spiral lamina.

378 Future work will be required to identify the RTN4RL2 ligands in the cochlea. To this
379 date, the interaction partners of RTN4Rs are not very well understood. While RTN4R in-trans
380 interactions include NogoA, MAG, OMgp, chondroitin sulfate proteoglycans, the only well
381 established ligand for RTN4RL2 remains MAG (Fournier et al., 2001; Domeniconi et al., 2002;
382 Wang et al., 2002a; Venkatesh et al., 2005; Schwab, 2010). Other attractive candidate ligands
383 for RTN4Rs are the BAIs. BAI-RTN4R interaction has been suggested to mediate dendritic
384 arborization, axonal elongation, synapse formation in IPSCs (Wang et al., 2021) and, in the
385 case of this study GluA2/3 AMPA receptor subunit localization to the SGN postsynaptic
386 densities. Finally, RTN4RL2 has been proposed to interact with chondroitin-sulfate
387 proteoglycan Versican to control the amount of skin innervation by DRG neurites (Bäumer et
388 al., 2014). While to our knowledge, attempts have yet to be made for detecting Versican signal
389 around the IHCs, other extracellular matrix proteins such as aggrecan, brevican, Tenascin-R,
390 Tenascin-C, hyaluron and proteoglycan link proteins 1 and 4 have been shown to form dense,
391 basket-like structures that surround the base of the IHCs (Kwiatkowska et al., 2016; Sonntag
392 et al., 2018). Furthermore, deletion of brevican results in alteration of pre- and postsynaptic
393 spatial coupling at IHC synapses, indicating the possible role of extracellular matrix in
394 transsynaptic organization. However, while the existing observations suggest that the synaptic
395 changes in RTN4RL2 deficient animals might reflect derailed interaction of the SGN neurites
396 with the extracellular matrix, the relevance of such an interaction of RTN4RL2 and Versican in
397 the cochlea needs to be addressed in the future.

398

399 # Materials and Methods
400
401 ## Animals
402
403 RTN4RL2 null mutant mice on a C57BL/6N background were generated as previously
404 described (Wörter et al., 2009). Knock-out (RTN4RL2$^{-/-}$) and wild-type (RTN4RL2$^{+/+}$) mice were
405 derived from heterozygous matings. Both male and female mice were used in this study.
406 Animals were genotyped as previously described (Wörter et al., 2009). The ages of the mice
407 varied depending on the experiment as noted in the manuscript. The breeding and the
408 experiments were approved by the Institutional Animal Care and Use Committee at
409 the Medical University of Innsbruck, local Animal Welfare Committee of the University
410 Medical Center Göttingen and the Max Planck Institute for Multidisciplinary Sciences, as well
411 as the Animal Welfare Office of the state of Lower Saxony, Germany (LAVES, AZ: 19/3134).
412 The ABR experiments were carried out under the approval of the Austrian Ministry of
413 Education, Science and Research (reference number BMWFW-66.011/0120-WF/V/3b/2016).
414
415 ## Patch-clamp recordings
416
417 The apical turn of the organ of Corti was dissected from p21 to p29 animals in HEPES Hanks
418 solution containing (in mM): 5.36 KCl, 141.7 NaCl, 10 HEPES, 0.5 $MgSO_4$, 1 $MgCl_2$, 5.6 D-
419 glucose, and 3.4 L-glutamine (pH 7.2, ~ 300 mOsm/l). IHCs were exposed by gently removing
420 of nearby supporting cells by negative pressure through a glass pipette from either modiolar
421 or pillar side. All experiments were conducted at room temperature (RT, 20–25°C). Patch
422 pipettes were made from GB150-8P or GB150F-8P borosilicate glass capillaries (Science
423 Products, Hofheim, Germany) for perforated and ruptured patch-clamp configurations,
424 respectively. Pipettes were fire polished with a custom-made microforge and coated with
425 Sylgard to minimize the capacitive noise, whenever capacitance recordings were performed.
426 The measurements were performed using EPC-10 amplifier controlled by Patchmaster
427 software (HEKA Elektronik, Germany). The holding potential for IHCs was set to -87 mV across
428 all the experiments.
429
430 ### Ruptured patch-clamp
431

432 For ruptured patch-clamp we used extracellular solution containing (in mM): 2.8 KCl, 105 NaCl,
433 10 HEPES, 1 CsCl, 1 $MgCl_2$, 5 $CaCl_2$, 35 TEA-Cl, and 2 mg/ml D-glucose (pH 7.2, ~ 300 mOsm/l).
434 Intracellular solution contained in mM: 111 Cs-glutamate, 1 $MgCl_2$, 1 $CaCl_2$, 10 EGTA, 13 TEA-
435 Cl, 20 HEPES, 4 Mg-ATP, 0.3 Na-GTP and 1 L-glutathione (pH 7.3, ~ 290 mOsm/l). Additionally,
436 Ca^{2+} indicator Fluo4-FF (0.8 mM, Life Technologies) and TAMRA-conjugated RIBEYE/Ctbp2
437 binding peptide (10 mM, synthetized by the group of Dr. Olaf Jahn, Göttingen) were added to
438 the intracellular solution for live imaging (Zenisek et al., 2004). Voltage dependency of Ca^{2+}
439 influx was recorded by applying 20 ms long step deploarizations with 5 mV increment. For
440 Ca^{2+} imaging, voltage ramp depolarizations ranging from -87 mV to 63 mV in the course of 150
441 ms were applied to the cells. Leak correction was performed using P/n protocol and liquid
442 junction potential of 17 mV was corrected offline. Recordings were discarded from the
443 analysis if the series resistance (R_s) exceeded 14 MOhm during the first 3 minutes after
444 rupturing the cell, leak current exceeded -50 pA at the holding potential and Ca^{2+} current
445 rundown was more than 25%.
446 Recordings were analyzed using Igor Pro 6.3 (Wavemetrics) custom-written programs. Ca^{2+}
447 current-voltage relationships (IV curves) were obtained by averaging approximately 5 ms
448 segments at the maximal activation regions of individual current traces and plotting them
449 against the depolarization voltages. Fractional activation curves of the Ca^{2+} channels were
450 calculated from the IVs and fitted with the Boltzmann function to determine the voltage of
451 half maximal activation (V_{half}) and voltage sensitivity (k).
452

453 ## Perforated patch clamp recordings
454

455 To perform simultaneous membrane capacitance (C_m) and Ca^{2+} current measurements we
456 used extracellular solution containing (in mM): 106 NaCl, 35 TEA-Cl, 2.8 KCl, 1 $MgCl_2$, 1 CsCl,
457 10 HEPES, 3 $CaCl_2$, and 5.6 D-glucose (pH 7.2, ~ 300 mOsm/l). The pipette solution contained
458 (in mM): 137 Cs-gluconate, 15 TEA-Cl, 3 GTP-Na_2, 1 ATP-Mg, 10 HEPES, 1 $MgCl_2$, as well as 300
459 mg/ml amphotericin B (pH 7.17, ~ 290 mOsm/l). Perforated patch-clamp recordings from
460 IHCs was described previously (Moser and Beutner, 2000). C_m changes were measured using
461 Lindau-Neher technique (Lindau and Neher, 1988). To evoke exocytosis IHCs were stimulated
462 by step depolarizations (to -17 mV) of different durations (2, 5, 10, 20, 50, 100 ms) in
463 randomized manner. Currents were leak-corrected using a p/5 protocol. Recordings were used

464 only if the leak current was lower than 30 pA and the R_s was lower than 30 MOhm. Recordings
465 were analyzed using Igor Pro 6.3 (Wavemetrics) custom-written programs. Ca^{2+} charge ($Q_{Ca}{}^{2+}$)
466 was calculated by the time integral of the leak-subtracted Ca^{2+} current during the
467 depolarization step. ΔC_m was calculated as the difference between the average C_m before and
468 after the depolarization. To measure average C_m we used 400 ms segments and skipped the
469 initial 100 ms after the depolarization.

470

471 ## Ca^{2+} imaging

472

473 Ca^{2+} imaging was performed using spinning disc confocal microscope, as described before
474 (Ohn et al., 2016). Briefly, the set-up was equipped with a spinning disc confocal unit (CSU22,
475 Yokogawa) mounted on an upright microscope (Axio Examiner, Zeiss) and scientific CMOS
476 camera (Andor Neo). Images were acquired using 63x, 1.0 NA objective (W Plan-Apochromat,
477 Zeiss). The pixel size was measured to be 103 nm.
478 IHCs were loaded with Fluo4-FF Ca^{2+} dye and TAMRA-conjugated Ctbp2 binding dimeric
479 peptide via the patch pipette. First, the cells were scanned from bottom to top by imaging
480 TAMRA fluorescence with 561 nm laser (Jive, Cobolt AB) and exposing each plane for 0.5
481 seconds. The stack was acquired with 0.5 μm step size using Piezo positioner (Piezosystem).
482 This allowed us to identify the planes containing synaptic ribbons. Next, we recorded Fluo4-
483 FF fluorescence increase at individual synapses by imaging ribbon containing planes with 491
484 nm laser (Calypso, Cobolt AB) at 100 Hz while applying voltage ramp depolarizations to the
485 cell. 2 voltage ramps were applied at each plane, one being 5 ms shifted relative to the other.
486 Spinning disk rotation speed was set to 2000 rpm, in order to synchronize with Ca^{2+} imaging.
487 Images were analyzed using Igor Pro 6.3 (Wavemetrics). Ca^{2+} hotspots were identified by
488 subtracting the average signal of several baseline frames from the average signal of 5 frames
489 during stimulation (ΔF image). Since the same Ca^{2+} hotspot appears across multiple planes,
490 the plane exhibiting the strongest signal was chosen. The intensities of the 3x3 matrix
491 surrounding the central pixel of the hotspot were averaged across all time points to obtain the
492 intensity profiles of Ca^{2+} influx over time. Afterwards, the background signal (average of
493 approximately 60x60 pixel intensities outside the cell) was subtracted from the intensity-time
494 profiles and $\Delta F/F_0$ traces were calculated. To enhance voltage resolution of Ca^{2+} imaging, two
495 $\Delta F/F_0$ traces corresponding to two voltage ramp depolarizations (one shifted by 5 ms over the

496 other) were combined and plotted against the corresponding voltages (FV curves). These
497 curves were subsequently fitted with a modified Boltzmann function. Afterwards, fractional
498 activation curves were calculated by fitting the linear decay of the fluorescence signal from
499 the FV curves with a linear function (G_{max}) and then dividing the FV fit by the G_{max} line. The
500 resulting curves were further fitted with a Boltzmann function. Maximal Ca^{2+} influx ($\Delta F/F_{0\ max}$)
501 was calculated by averaging 5 points during the stimulation.
502
503 ## Immunohistochemistry
504
505 Amplified immunohistochemistry for RTN4RL2 was performed on 5 μm dewaxed paraffin
506 sections of RTN4RL2$^{+/+}$ and RTN4RL2$^{-/-}$ inner ears from either sex. All tissue sections were
507 incubated in 10 mM sodium citrate buffer (pH = 6) at 98°C for 10 min, washed in PBS, and
508 endogenous peroxidase quenched using 3% H_2O_2, in 1X PBS for 10 min. Tissue was blocked in
509 2% normal goat serum, 1% BSA and 0.3% Triton-X100 in PBS for 2 hours at RT, followed by
510 overnight incubation with primary rabbit anti-RTN4RL2 (1:400, Invitrogen, PA598577) at 4°C.
511 Biotin-labelled goat anti-rabbit (2 hours at RT; 1:500, Ba-1000, Vector Laboratories) and the
512 ImmPACT DAB Kit (SK-4105, Vector Laboratories) were used for signal detection. After several
513 washes, sections were incubated with TSA plus Cyanine-3 reagent (1:2000, NEL760001KT,
514 Perkin Elmer) for 10 to 15 min at RT in accordance with the manufacturer's protocol.
515 Subsequently, sections were stained overnight with mouse anti-βIII-tubulin (1:1000, 801202,
516 Biolegend) at 4°C, followed by secondary Alexa Fluor 488 conjugated goat anti-mouse (1:1000,
517 Thermo Fisher Scientific), for 2 hours at RT. Finally, sections were cover slipped in Mowiol and
518 stored at 4°C until imaging.
519 For whole mount immunofluorescence, cochleae were fixed in 4% formaldehyde on ice for
520 45-60 minutes or sometimes overnight. For anti-$Ca_V1.3$ stainings the cochleae were fixed for
521 10 minutes. After the fixation, the organs of Corti were microdissected in PBS and blocked in
522 GSDB (goat serum dilution buffer; 16% goat serum, 20 mM phosphate buffer (PB), 0.3% Triton
523 X-100, 0.45 M NaCl) for 1 hour at RT. The samples were then incubated in the primary antibody
524 mixture overnight at 4°C. The next day, samples were washed 3 times using wash buffer (20
525 mM PB, 0.3% Triton X-100, 0.45 M NaCl) followed by incubation in the secondary antibody
526 mixture for 1 hour at RT. Afterwards, the samples were washed 3 times in the washing buffer,
527 one time in PB and mounted using mounting medium (Mowiol).

528 The following primary antibodies were used: rabbit anti-Homer1 (1:500, 160 002, Synaptic
529 Systems), mouse anti-Ctbp2 (1:200, 612044, BD Biosciences), rabbit anti-$Ca_V1.3$ (1:100, ACC-
530 005, Alomone Labs), mouse anti-Bassoon (1:300, ab82958, Abcam), rabbit anti-Myosin7a
531 (1:800, ab3481, Abcam, or Proteus BioScience), guinea pig anti-RibeyeA (1:500, 192104,
532 Synaptic Systems), guinea pig anti-Synapsin1/2 (1:500, 106004, Synaptic Systems), guinea pig
533 anti-Vglut3 (1:500, 135204, Synaptic Systems), chicken anti-parvalbumin (1:200, 195006,
534 Synaptic Systems), chicken anti-calretinin (1:200, 214 106, Synaptic Systems), guinea pig anti-
535 VAChT (1:1000, 139105, Synaptic Systems), mouse anti-ATP1A3 (1:300, MA3-915, Thermo
536 Fisher Scientific).
537 The following secondary antibodies were used: Alexa Fluor 488 conjugated anti-guinea pig
538 (1:200, A11073, Thermo Fisher Scientific), Alexa Fluor 488 conjugated anti-rabbit (1:200,
539 A11008, Thermo Fisher Scientific), Alexa Fluor 568 conjugated anti-chicken (1:200, ab175711,
540 Abcam), Alexa Fluor 633 conjugated anti-guinea pig (1:200, A21105, Thermo Fisher Scientific),
541 STAR 580 conjugated anti-mouse (1:200, Abberior, ST635P-1001-500UG), STAR 635
542 conjugated anti-rabbit (1:200, Abberior, ST635P-1002-500UG).
543 Confocal stacks were acquired using Leica SP8 confocal microscope or Abberior Instruments
544 Expert Line STED microscope.
545 The volumes of the Ctbp2 and Homer1 positive puncta were estimated using the surface
546 algorithm of Imaris software (version 9.6.0, Bitplane). Following parameters were used to
547 create the surfaces for both Ctbp2 and Homer1 puncta in all the analyzed stacks: surface detail
548 0.07 μm, background subtraction 0.562 μm, touching object size 0.4 μm.
549 The brightness and the contrast of the representative images were adjusted using Fiji (ImageJ)
550 software for the visualization purposes.
551

552 ## Spiral ganglion neuron densities

553
554 $RTN4RL2^{+/+}$ and $RTN4RL2^{-/-}$ cochlea from p40 mice of either sex were processed for SGN
555 counts. Mouse monoclonal anti-βIII-tubulin (1:1000, 801202, Biolegend) at 4°C, followed by
556 secondary Alexa Fluor 488 conjugated anti-mouse (1:1000, Thermo Fisher Scientific), was
557 used to label all SGNs. Nuclei were visualized using a DAPI fluorescent counterstain (1:1000,
558 Life Technologies). 20X images of mid-modiolar cochlear sections were collected. ImageJ was
559 used to outline the spiral ganglion and generate the area. Quantitative assessment was

560 performed on every other mid-modiolar section to reduce chances of double counting.
561 Labeled cells were counted only if they had a round cell body, presence of nucleus, and
562 homogenous cytoplasm. Densities were calculated and statistical differences were measure
563 using a Student's t-test (GraphPad Prism, GraphPad Software Inc.).

564

565 ## Inner and outer Hair cell counts

566

567 IHC and OHC counts were performed for RTN4RL2$^{+/+}$ and RTN4RL2$^{-/-}$ mice at the ages of p15,
568 1 month and 2 months. Images were imported to ImageJ software, where IHC/OHC counts
569 were performed blinded to genotype using the 'Cell counter' tool. To quantify the cells the
570 nuclear staining of the DAPI channel was used. The number of IHCs and OHCs was assessed
571 along a length of 100 μm for each image, and then averaged across all samples to obtain the
572 average number of IHCs (or OHCs) per 100 μm.

573

574 ## RNAscope

575

576 RNA *in-situ* hybridization was performed using RNAscope® (Advanced Cell Diagnostics).
577 Standard mouse probes were used to examine the expression of RTN4RL2 (450761, ACD) and
578 Gria2 (865091, ACD) closely following the manufacturer's instructions. Briefly, 6 mm paraffin
579 tissue sections underwent deparaffinization with xylene and a series of ethanol washes.
580 Tissues were heated in kit-provided antigen retrieval buffer and digested by kit-provided
581 proteinase. Sections were exposed to mFISH target probes and incubated at 40°C in a
582 hybridization oven for 2 hours. After rinsing, mFISH signal was amplified using company-
583 provided pre-amplifier and amplifier conjugated to fluorescent dye. Subsequently, sections
584 were blocked with 1% BSA, 2% normal goat serum in 1xPBS containing 0.3% Triton X-100 for
585 1 hour at RT. The tissue was incubated in mouse anti-βIII-tubulin antibody (1:500, 801202,
586 Biolegend) overnight at 4°C. The next day, sections were rinsed with PBS, blocked again before
587 incubating in secondary Alexa Fluor 488 conjugated anti-mouse antibody (1:1000, Invitrogen)
588 for 2 hours at RT. Sections were counterstained with DAPI (1:1000, Life Technologies),
589 mounted, and stored at 4°C until image analysis. mFISH images were captured on a Leica SP8
590 confocal microscope and processed using ImageJ.

591

592

593 ## Serial block-face scanning electron microscopy (SBEM)

594

595 ### Sample preparation for SBEM

596

597 One RTN4RL2$^{+/+}$ and two RTN4RL2$^{-/-}$ female mice at p36 were used for the SBEM experiments.
598 Cochleae were processed for SBEM imaging as previously described (Hua et al., 2021).
599 In brief, the animals were decapitated after CO_2 inhalation under anesthesia. The cochleae
600 were dissected from the skulls and immediately fixed by perfusing with ice-cold fixative
601 through the round and oval windows at constant flow speed using an infusion pump (Micro4,
602 WPI). The fixative solution was freshly prepared and made of 4% paraformaldehyde (Sigma-
603 Aldrich), 2.5% glutaraldehyde (Sigma-Aldrich), and 0.08 M cacodylate (pH 7.4, Sigma-Aldrich).
604 After being immersed in the fixative at 4°C for 5 hours, the cochleae were transferred to a
605 decalcifying solution containing the same fixative and 5% ethylenediaminetetraacetic acid
606 (EDTA, Serva) and incubated at 4°C for 5 hours. The samples were then washed twice with
607 0.15 M cacodylate (pH 7.4) for 30 min each, sequentially immersed in 2% OsO_4 (Sigma-
608 Aldrich), 2.5% ferrocyanide (Sigma-Aldrich), and again 2% OsO_4 at RT for 2, 2, and 1.5 hours.
609 After being washed in 0.15 M cacodylate and distilled water (Sartorius) for 30 min each, the
610 samples were sequentially incubated in filtered 1% thiocarbohydrazide (TCH, Sigma-Aldrich)
611 solution and 2% OsO_4 at RT for 1 and 2 hours, as well as in lead aspartate solution (0.03 M, pH
612 5.0, adjusted with KOH) at 50 °C for 2 hours with immediate two washing steps with distilled
613 water at RT for 30 min each. For embedding, the samples were dehydrated through graded
614 pre-cooled acetone (Carl Roth) series (50%, 75%, 90%, for 30 min each, all cooled at 4 °C) and
615 then pure acetone at RT (three times for 30 min each). The sample infiltration started with 1:1
616 and 1:2 mixtures of acetone and Spurr's resin monomer (4.1 g ERL 4221, 0.95 g DER 736, 5.9
617 g NSA and 1% DMAE; Sigma-Aldrich) at RT for 6 and 12 hours on a rotator. After being
618 impregnated in pure resin for 12 hours, the samples were placed in embedding molds
619 (Polyscience) and hardened in a pre-warmed oven at 70°C for 72 hours.

620

621 ### Sample trimming and SBEM imaging

622

623 The sample blocks were mounted upright along the conical center axis on aluminum metal
624 rivets (3VMRS12, Gatan, UK) and trimmed coronally towards the modiolus using a diamond
625 trimmer (TRIM2, Leica, Germany). For each sample, a block face of about ~ 600 x 800 mm^2,

626 centered at the apical segment based on the anatomical landmarks, was created using an
627 ultramicrotome (UC7, Leica, Germany). The samples were coated with a 30 nm thick gold layer
628 using a sputter coater (ACE600, Leica, Germany). The serial images were acquired using a field-
629 emission scanning EM (Gemini300, Carl Zeiss, Germany) equipped with an in-chamber
630 ultramicrotome (3ViewXP, Gatan, UK) and back-scattered electron detector (Onpoint, Gatan,
631 UK). Focal charge compensation was set to 100 % with a high vacuum chamber pressure of
632 2.8 x 10^3 mbar. The following parameters were set for the SBEM imaging: 12 nm pixel size, 50
633 nm nominal cutting thickness, 2 keV incident beam energy, and 1.5 ms pixel dwell time.
634 For the RTN4RL2$^{+/+}$ dataset, 2377 consecutive slices (9000 × 15000 pixels) were collected,
635 whereas the two RTN4RL2$^{-/-}$ datasets had 3217 slices (16000 × 10000 pixels) and 2425 slices
636 (9000 × 15000 pixels). All datasets were aligned along the z-direction using a custom MATLAB
637 script based on cross-correlation maximum between consecutive slices (Hua et al., 2022)
638 before being uploaded to webKnossos (Boergens et al., 2017) for skeleton and volume tracing.
639

640 ### Identification and quantification of auditory afferent fibers

641
642 In our SBEM datasets of the cochlea, manual skeleton tracing was carried out on all neurites
643 that originated from three neighboring habenula perforata (HP) at the center of each dataset.
644 To search for type I afferent fibers, several morphological features were used, such as
645 myelination after entering HP, radial and unbranched fiber trajectory, contact with IHCs, as
646 well as ribbon-associated terminals (Hua et al., 2021). This resulted in 115 putative type I
647 afferent fibers and further classification was made based on the presence of presynaptic
648 ribbon, fiber branching, and contact with IHC. For an illustration purpose, a type I afferent
649 fiber bundle of one RTN4RL2$^{-/-}$ dataset was volume traced and 3D rendered using Amira
650 software (Thermo Scientific, US).
651

652 ### Ribbon size measurement and synapse counting

653
654 Ribbon-type synapses were manually annotated in 18 intact IHCs captured by SBEM using
655 webKnossos. The dense core region of individual ribbon synapses was manually contoured,
656 and the associated voxels were counted for ribbon volume measurement. In the case of multi-
657 ribbon synapses, all ribbon bodies at a single active zone were summed up to yield the ribbon
658 volume.

Auditory brainstem responses

Auditory brainstem resposes (ABR) were recorded in 2-4 months old mice of either sex, as described previously (Luque et al., 2021). Briefly, we used a custom-made system in an anechoic chamber in a calibrated open-field configuration. ABRs were recorded via needle electrodes in response to tone bursts of 4, 8, 16, and 32 kHz or a click wide spectrum (2-45,2 KHz, 2 KHz steps) as stimuli. Tone pips of 3 ms duration (1 ms rise and fall time) were presented at a rate of 60/s with alternating phases. Starting with 0 dB, the stimuli were increased in 5 dB steps up to 120 dB. Hearing thresholds were determined as the minimum stimulation level that produced a clearly recognizable potential. Recordings were evaluated by three independent researchers in a blinded manner.

Data analysis and statistics

The data were analyzed using Igor Pro (Wavemetrics), Python and GraphPad Prism (GraphPad Software Inc.) software. For 2 sample comparisons, data were tested for normality and equality of variances using Jarque-Bera and F-test, respectively. Afterwards, two-tailed Student's t-test or Mann-Whitney-Wilcoxon test were performed. The latter was used when normality and/or equality of variances were not met. P-values were corrected for multiple comparisons using Holm-Šídák method. For ABR thresholds Kruskal-Wallis test followed by Dunn's multiple comparison test was used. Data is presented as mean ± standard error of the mean (SEM), unless otherwise stated. Significances are reported as *$p < 0.05$, **$p < 0.01$, ***$p < 0.001$. The number of the animals is indicated as N.

Acknowledgements

We thank Sina Langer, Christiane Senger-Freitag, Sandra Gerke for expert technical support. We thank Prof. Dr. Carolin Wichmann, Dr. Susann Michanski, Julius Bahr and Sophia Mutschall for the help with the SBEM sample preparation. We thank Dr. Yi Jiang and Haoyu Wang for the visualization of neurite reconstruction. We would also like to thank Prof. Dr. Olaf Jahn and Lars van Werven for the TAMRA-conjugated Ctbp2 binding peptide synthesis. The study was supported by German Research Foundation through the Cluster of Excellence (EXC2067) Multiscale Bioimaging (TM) and the Leibniz Program (MO896/5 to TM) as well as by the

European Research Council through the Advanced Grant “DynaHear” to TM under the European Union’s Horizon 2020 Research and Innovation program (grant agreement No. 101054467), and by Fondation Pour l’Audition (FPA RD-2020-10), by the SPIN-FWF grant to CB, and by the National Natural Science Foundation of China (82171133 to YH), Industrial Support Fund of Huangpu District .in Shanghai (XK2019011 to YH), Innovative Research Team of High-level Local Universities in Shanghai (SHSMU-ZLCX20211700). NK is a member of the Hertha Sponer College from the Cluster of Excellence Multiscale Bioimaging (MBExC). TM is a Max-Planck Fellow at the Max Planck Institute for Multidisciplinary Sciences.

Author contributions

CB, TM, YH, and NK designed the research. NK, MÜ, YQ, NB, FH, LJC, FW, ML, RG performed experiments and analyzed data. NK and TM wrote the paper with contributions of YH, CB, YQ, NB. CB, TM, YH acquired funding. All authors have reviewed and approved the final version of the manuscript for submission.

References

Appler, J. M., and Goodrich, L. V. (2011). Connecting the ear to the brain: Molecular mechanisms of auditory circuit assembly. *Prog. Neurobiol.* 93, 488–508. doi: 10.1016/j.pneurobio.2011.01.004

Bäumer, B. E., Kurz, A., Borrie, S. C., Sickinger, S., Dours-Zimmermann, M. T., Zimmermann, D. R., et al. (2014). Nogo receptor homolog NgR2 expressed in sensory DRG neurons controls epidermal innervation by interaction with Versican. *J. Neurosci. Off. J. Soc. Neurosci.* 34, 1633–1646. doi: 10.1523/JNEUROSCI.3094-13.2014

Boergens, K. M., Berning, M., Bocklisch, T., Bräunlein, D., Drawitsch, F., Frohnhofen, J., et al. (2017). webKnossos: efficient online 3D data annotation for connectomics. *Nat. Methods* 14, 691–694. doi: 10.1038/nmeth.4331

Borrie, S. C., Sartori, S. B., Lehmann, J., Sah, A., Singewald, N., and Bandtlow, C. E. (2014). Loss of Nogo receptor homolog NgR2 alters spine morphology of CA1 neurons and emotionality in adult mice. *Front. Behav. Neurosci.* 8. Available at: https://www.frontiersin.org/articles/10.3389/fnbeh.2014.00175 (Accessed March 1, 2024).

Bulankina, A. V., and Moser, T. (2012). Neural circuit development in the mammalian cochlea. *Physiology* 27, 100–112. doi: 10.1152/physiol.00036.2011

Cantu-Guerra, H. L., Papazian, M. R., Gorsky, A. L., Alekos, N. S., Caccavano, A., Karagulyan, N., et al. (2023). Cochlear hair cell innervation is dependent on a modulatory function of Semaphorin-3A. *Dev. Dyn.* 252, 124–144. doi: 10.1002/dvdy.548

Carlton, A. J., Jeng, J.-Y., Grandi, F. C., De Faveri, F., Amariutei, A. E., De Tomasi, L., et al. (2024). BAI1 localizes AMPA receptors at the cochlear afferent post-synaptic density and is essential for hearing. *Cell Rep.* 43, 114025. doi: 10.1016/j.celrep.2024.114025

Coate, T. M., Scott, M. K., and Gurjar, M. (2019). Current concepts in cochlear ribbon synapse formation. *Synapse* 73, e22087. doi: 10.1002/syn.22087

Coate, T. M., Spita, N. A., Zhang, K. D., Isgrig, K. T., and Kelley, M. W. (2015). Neuropilin-2/Semaphorin-3F-mediated repulsion promotes inner hair cell innervation by spiral ganglion neurons. *eLife* 4. doi: 10.7554/eLife.07830

Defourny, J., Poirrier, A.-L., Lallemend, F., Mateo Sánchez, S., Neef, J., Vanderhaeghen, P., et al. (2013). Ephrin-A5/EphA4 signalling controls specific afferent targeting to cochlear hair cells. *Nat. Commun.* 4, 1438. doi: 10.1038/ncomms2445

Domeniconi, M., Cao, Z., Spencer, T., Sivasankaran, R., Wang, K. C., Nikulina, E., et al. (2002). Myelin-Associated Glycoprotein Interacts with the Nogo66 Receptor to Inhibit Neurite Outgrowth. *Neuron* 35, 283–290. doi: 10.1016/S0896-6273(02)00770-5

Elkon, R., Milon, B., Morrison, L., Shah, M., Vijayakumar, S., Racherla, M., et al. (2015). RFX transcription factors are essential for hearing in mice. *Nat. Commun.* 6, 8549. doi: 10.1038/ncomms9549

Fell, B., Eckrich, Stephanie, Hecker, Dietmar, Obermair, Gerald J., Flockerzi, V., Schick, B., et al. (2015). α2δ2 Controls the Function and Transsynaptic Coupling of Cav1.3 Channels in Mouse Inner Hair Cells and is Essential for Normal Hearing. *ARO Midwintermeeting*.

Fournier, A. E., GrandPre, T., and Strittmatter, S. M. (2001). Identification of a receptor mediating Nogo-66 inhibition of axonal regeneration. *Nature* 409, 341–346. doi: 10.1038/35053072

Hua, Y., Ding, X., Wang, H., Wang, F., Lu, Y., Neef, J., et al. (2021). Electron Microscopic Reconstruction of Neural Circuitry in the Cochlea. *Cell Rep.* 34, 108551. doi: 10.1016/j.celrep.2020.108551

Hua, Y., Loomba, S., Pawlak, V., Voit, K.-M., Laserstein, P., Boergens, K. M., et al. (2022). Connectomic analysis of thalamus-driven disinhibition in cortical layer 4. *Cell Rep.* 41, 111476. doi: 10.1016/j.celrep.2022.111476

Jaime Tobón, L. M., and Moser, T. (2023a). Bridging the gap between presynaptic hair cell function and neural sound encoding. doi: 10.7554/eLife.93749.1

Jaime Tobón, L. M., and Moser, T. (2023b). Ca2+ regulation of glutamate release from inner hair cells of hearing mice. *Proc. Natl. Acad. Sci.* 120, e2311539120. doi: 10.1073/pnas.2311539120

Jean, P., Morena, D. L. de la, Michanski, S., Tobón, L. M. J., Chakrabarti, R., Picher, M. M., et al. (2018). The synaptic ribbon is critical for sound encoding at high rates and with temporal precision. *eLife* 7, e29275. doi: 10.7554/eLife.29275

Jean, P., Wong Jun Tai, F., Singh-Estivalet, A., Lelli, A., Scandola, C., Megharba, S., et al. (2023). Single-cell transcriptomic profiling of the mouse cochlea: An atlas for targeted therapies. *Proc. Natl. Acad. Sci.* 120, e2221744120. doi: 10.1073/pnas.2221744120

Johnson, S. L., Safieddine, S., Mustapha, M., and Marcotti, W. (2019). Hair Cell Afferent Synapses: Function and Dysfunction. *Cold Spring Harb. Perspect. Med.* 9. doi: 10.1101/cshperspect.a033175

Jukic, A., Lei, Z., Cebul, E. R., Pinter, K., Mosqueda, N., David, S., et al. (2024). Presynaptic Nrxn3 is essential for ribbon-synapse assembly in hair cells. doi: 10.1101/2024.02.14.580267

Jung, J. S., Zhang, K. D., Wang, Z., McMurray, M., Tkaczuk, A., Ogawa, Y., et al. (2019). Semaphorin-5B Controls Spiral Ganglion Neuron Branch Refinement during Development. *J. Neurosci.* 39, 6425–6438. doi: 10.1523/JNEUROSCI.0113-19.2019

Koundakjian, E. J., Appler, J. L., and Goodrich, L. V. (2007). Auditory neurons make stereotyped wiring decisions before maturation of their targets. *J. Neurosci. Off. J. Soc. Neurosci.* 27, 14078–14088. doi: 10.1523/JNEUROSCI.3765-07.2007

Kujawa, S. G., and Liberman, M. C. (2009). Adding insult to injury: cochlear nerve degeneration after “temporary” noise-induced hearing loss. *J. Neurosci.* 29, 14077.

Kujawa, S. G., and Liberman, M. C. (2015). Synaptopathy in the noise-exposed and aging cochlea: Primary neural degeneration in acquired sensorineural hearing loss. *Hear. Res.* 330, 191–199. doi: 10.1016/j.heares.2015.02.009

Kwiatkowska, M., Reinhard, J., Roll, L., Kraft, N., Dazert, S., Faissner, A., et al. (2016). The expression pattern and inhibitory influence of Tenascin-C on the growth of spiral ganglion neurons suggest a regulatory role as boundary formation molecule in the postnatal mouse inner ear. *Neuroscience* 319, 46–58. doi: 10.1016/j.neuroscience.2016.01.039

Liberman, L. D., and Liberman, M. C. (2016). Postnatal maturation of auditory-nerve heterogeneity, as seen in spatial gradients of synapse morphology in the inner hair cell area. *Hear. Res.* 339, 12–22. doi: 10.1016/j.heares.2016.06.002

Lindau, M., and Neher, E. (1988). Patch-clamp techniques for time-resolved capacitance measurements in single cells. *Pflüg. Arch. Eur. J. Physiol.* 411, 137–146.

Liu, H., Chen, L., Giffen, K. P., Stringham, S. T., Li, Y., Judge, P. D., et al. (2018). Cell-Specific Transcriptome Analysis Shows That Adult Pillar and Deiters’ Cells Express Genes Encoding Machinery for Specializations of Cochlear Hair Cells. *Front. Mol. Neurosci.* 11. doi: 10.3389/fnmol.2018.00356

Lu, Y., Liu, J., Li, B., Wang, H., Wang, F., Wang, S., et al. (2024). Spatial patterns of noise-induced inner hair cell ribbon loss in the mouse mid-cochlea. *iScience* 27, 108825. doi: 10.1016/j.isci.2024.108825

Luque, M., Schrott-Fischer, A., Dudas, J., Pechriggl, E., Brenner, E., Rask-Andersen, H., et al. (2021). HCN channels in the mammalian cochlea: Expression pattern, subcellular location, and age-dependent changes. *J. Neurosci. Res.* 99, 699–728. doi: 10.1002/jnr.24754

Matsubara, A., Laake, J. H., Davanger, S., Usami, S., and Ottersen, O. P. (1996). Organization of AMPA receptor subunits at a glutamate synapse: a quantitative immunogold analysis of hair cell synapses in the rat organ of Corti. *J. Neurosci.* 16, 4457.

Meyer, A. C., and Moser, T. (2010). Structure and function of cochlear afferent innervation. *Curr. Opin. Otolaryngol. Head Neck Surg.* 18, 441–446. doi: 10.1097/MOO.0b013e32833e0586

Michanski, S., Smaluch, K., Steyer, A. M., Chakrabarti, R., Setz, C., Oestreicher, D., et al. (2019). Mapping developmental maturation of inner hair cell ribbon synapses in the

apical mouse cochlea. *Proc. Natl. Acad. Sci.* 116, 6415–6424. doi: 10.1073/pnas.1812029116

Mironova, Y. A., and Giger, R. J. (2013). Where no synapses go: gatekeepers of circuit remodeling and synaptic strength. *Trends Neurosci.* 36, 363–373. doi: 10.1016/j.tins.2013.04.003

Moser, T., and Beutner, D. (2000). Kinetics of exocytosis and endocytosis at the cochlear inner hair cell afferent synapse of the mouse. *Proc. Natl. Acad. Sci.* 97, 883–888. doi: 10.1073/pnas.97.2.883

Moverman, D. J., Liberman, L. D., Kraemer, S., Corfas, G., and Liberman, M. C. (2023). Ultrastructure of noise-induced cochlear synaptopathy. *Sci. Rep.* 13, 19456. doi: 10.1038/s41598-023-46859-6

Niedzielski, A. S., and Wenthold, R. J. (1995). Expression of AMPA, kainate, and NMDA receptor subunits in cochlear and vestibular ganglia. *J. Neurosci.* 15, 2338.

Ohn, T.-L., Rutherford, M. A., Jing, Z., Jung, S., Duque-Afonso, C. J., Hoch, G., et al. (2016). Hair cells use active zones with different voltage dependence of Ca^{2+} influx to decompose sounds into complementary neural codes. *Proc. Natl. Acad. Sci.* 113, E4716–E4725. doi: 10.1073/pnas.1605737113

Özçete, Ö. D., and Moser, T. (2021). A sensory cell diversifies its output by varying Ca^{2+} influx-release coupling among active zones. *EMBO J.* 40, e106010. doi: 10.15252/embj.2020106010

Ramirez, M. A., Ninoyu, Y., Miller, C., Andrade, L. R., Edassery, S., Bomba-Warczak, E., et al. (2022). Cochlear ribbon synapse maturation requires Nlgn1 and Nlgn3. *iScience* 25, 104803. doi: 10.1016/j.isci.2022.104803

Roux, I., Safieddine, S., Nouvian, R., Grati, M., Simmler, M.-C., Bahloul, A., et al. (2006). Otoferlin, Defective in a Human Deafness Form, Is Essential for Exocytosis at the Auditory Ribbon Synapse. *Cell* 127, 277–289. doi: 10.1016/j.cell.2006.08.040

Ruel, J., Emery, S., Nouvian, R., Bersot, T., Amilhon, B., Van Rybroek, J. M., et al. (2008). Impairment of SLC17A8 Encoding Vesicular Glutamate Transporter-3, VGLUT3, Underlies Nonsyndromic Deafness DFNA25 and Inner Hair Cell Dysfunction in Null Mice. *Am. J. Hum. Genet.* 83, 278–292. doi: 10.1016/j.ajhg.2008.07.008

Rutherford, M. A., Bhattacharyya, A., Xiao, M., Cai, H.-M., Pal, I., and Rubio, M. E. (2023). GluA3 subunits are required for appropriate assembly of AMPAR GluA2 and GluA4 subunits on cochlear afferent synapses and for presynaptic ribbon modiolar-pillar morphology. *eLife* 12, e80950. doi: 10.7554/eLife.80950

Schwab, M. E. (2010). Functions of Nogo proteins and their receptors in the nervous system. *Nat. Rev. Neurosci.* 11, 799–811. doi: 10.1038/nrn2936

854 Seal, R. P., Akil, O., Yi, E., Weber, C. M., Grant, L., Yoo, J., et al. (2008). Sensorineural Deafness
855 and Seizures in Mice Lacking Vesicular Glutamate Transporter 3. *Neuron* 57, 263–275.
856 doi: 10.1016/j.neuron.2007.11.032

857 Sherrill, H. E., Jean, P., Driver, E. C., Sanders, T. R., Fitzgerald, T. S., Moser, T., et al. (2019).
858 Pou4f1 Defines a Subgroup of Type I Spiral Ganglion Neurons and Is Necessary for
859 Normal Inner Hair Cell Presynaptic Ca2+ Signaling. *J. Neurosci.* 39, 5284–5298. doi:
860 10.1523/JNEUROSCI.2728-18.2019

861 Shrestha, B. R., Chia, C., Wu, L., Kujawa, S. G., Liberman, M. C., and Goodrich, L. V. (2018).
862 Sensory Neuron Diversity in the Inner Ear Is Shaped by Activity. *Cell* 174, 1229-
863 1246.e17. doi: 10.1016/j.cell.2018.07.007

864 Shrestha, B. R., Wu, L., and Goodrich, L. V. (2023). Runx1 controls auditory sensory neuron
865 diversity in mice. *Dev. Cell* 58, 306-319.e5. doi: 10.1016/j.devcel.2023.01.008

866 Sonntag, M., Blosa, M., Schmidt, S., Reimann, K., Blum, K., Eckrich, T., et al. (2018). Synaptic
867 coupling of inner ear sensory cells is controlled by brevican-based extracellular
868 matrix baskets resembling perineuronal nets. *BMC Biol.* 16, 99. doi: 10.1186/s12915-
869 018-0566-8

870 Stephenson, J. R., Paavola, K. J., Schaefer, S. A., Kaur, B., Van Meir, E. G., and Hall, R. A.
871 (2013). Brain-specific Angiogenesis Inhibitor-1 Signaling, Regulation, and Enrichment
872 in the Postsynaptic Density. *J. Biol. Chem.* 288, 22248–22256. doi:
873 10.1074/jbc.M113.489757

874 Vaccaro, G., Dumoulin, A., Zuñiga, N. R., Bandtlow, C. E., and Stoeckli, E. T. (2022). The Nogo-
875 66 Receptors NgR1 and NgR3 Are Required for Commissural Axon Pathfinding. *J.*
876 *Neurosci.* 42, 4087–4100. doi: 10.1523/JNEUROSCI.1390-21.2022

877 Venkatesh, K., Chivatakarn, O., Lee, H., Joshi, P. S., Kantor, D. B., Newman, B. A., et al. (2005).
878 The Nogo-66 Receptor Homolog NgR2 Is a Sialic Acid-Dependent Receptor Selective
879 for Myelin-Associated Glycoprotein. *J. Neurosci.* 25, 808–822. doi:
880 10.1523/JNEUROSCI.4464-04.2005

881 Wang, J., Miao, Y., Wicklein, R., Sun, Z., Wang, J., Jude, K. M., et al. (2021). RTN4/NoGo-
882 receptor binding to BAI adhesion-GPCRs regulates neuronal development. *Cell* 184,
883 5869-5885.e25. doi: 10.1016/j.cell.2021.10.016

884 Wang, K. C., Koprivica, V., Kim, J. A., Sivasankaran, R., Guo, Y., Neve, R. L., et al. (2002a).
885 Oligodendrocyte-myelin glycoprotein is a Nogo receptor ligand that inhibits neurite
886 outgrowth. *Nature* 417, 941–944. doi: 10.1038/nature00867

887 Wang, X., Chun, S.-J., Treloar, H., Vartanian, T., Greer, C. A., and Strittmatter, S. M. (2002b).
888 Localization of Nogo-A and Nogo-66 Receptor Proteins at Sites of Axon–Myelin and
889 Synaptic Contact. *J. Neurosci.* 22, 5505–5515. doi: 10.1523/JNEUROSCI.22-13-
890 05505.2002

Wills, Z. P., Mandel-Brehm, C., Mardinly, A. R., McCord, A. E., Giger, R. J., and Greenberg, M. E. (2012). The Nogo Receptor Family Restricts Synapse Number in the Developing Hippocampus. *Neuron* 73, 466–481. doi: 10.1016/j.neuron.2011.11.029

Wong, A. B., Rutherford, M. A., Gabrielaitis, M., Pangršič, T., Göttfert, F., Frank, T., et al. (2014). Developmental refinement of hair cell synapses tightens the coupling of Ca2+ influx to exocytosis. *EMBO J.* 33, 247–264. doi: 10.1002/embj.201387110

Wörter, V., Schweigreiter, R., Kinzel, B., Mueller, M., Barske, C., Böck, G., et al. (2009). Inhibitory activity of myelin-associated glycoprotein on sensory neurons is largely independent of NgR1 and NgR2 and resides within Ig-Like domains 4 and 5. *PloS One* 4, e5218. doi: 10.1371/journal.pone.0005218

Zenisek, D., Horst, N. K., Merrifield, C., Sterling, P., and Matthews, G. (2004). Visualizing synaptic ribbons in the living cell. *J. Neurosci. Off. J. Soc. Neurosci.* 24, 9752–9759. doi: 10.1523/JNEUROSCI.2886-04.2004

Supplementary Figures

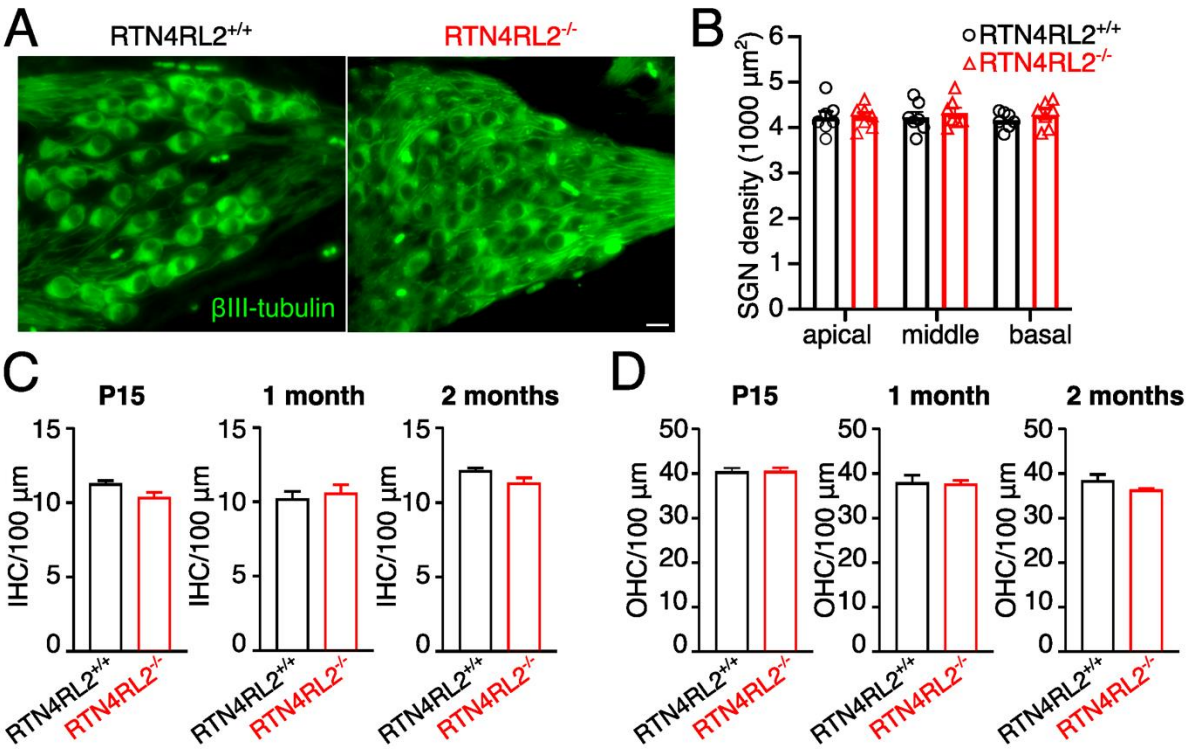

Figure 2-figure supplement 1. Cochlear cell densities are not changed in RTN4RL2$^{-/-}$ mice. (**A**) Mid/Basal-modiolar sections labeled for βIII-tubulin (green, neurons) from p40 RTN4RL2$^{+/+}$ and RTN4RL2$^{-/-}$ mice Exemplary section for RTN4RL2$^{-/-}$ is the zoomed out image presented in figure 1C. (**B**) Quantitative analysis shows that the density of SGN cell bodies are similar between RTN4RL2$^{-/-}$ and control cochleae. Data is presented as mean ± SD; N = 7 per group. Scale bar = 10 µm. (**C, D**) IHC (C) and OHC (D) densities are not affected in P15, 1 month and 2 months old RTN4RL2$^{-/-}$ mice.

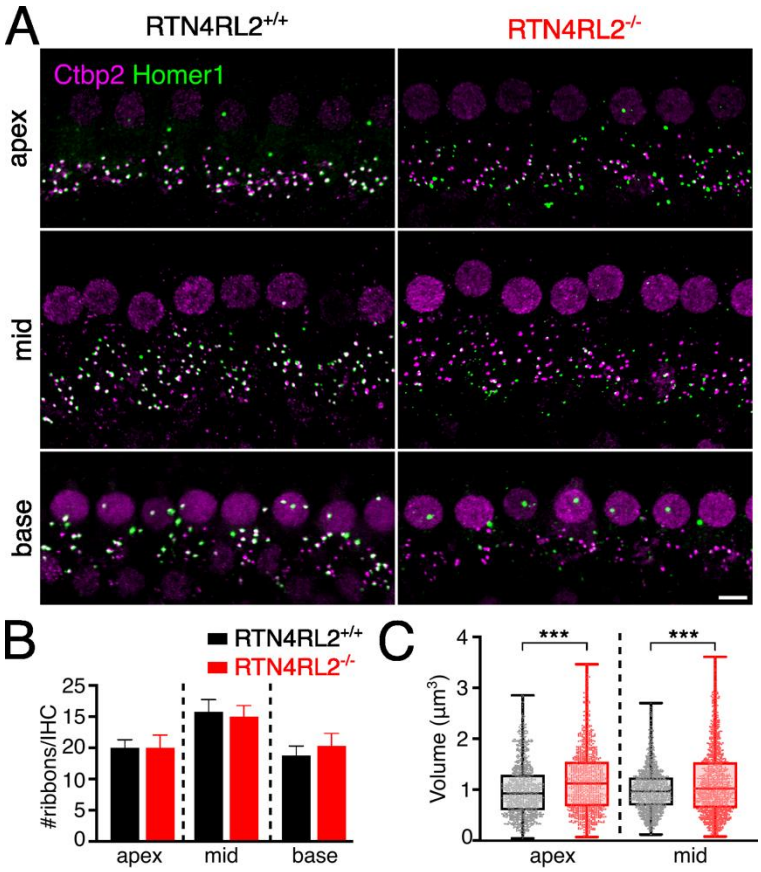

Figure 2-figure supplement 2. Intact number but enlarged size of the ribbons in RTN4RL2$^{-/-}$ IHCs. (**A**) Maximal intensity projections of representative IHCs from apical, mid and basal regions of RTN4RL2$^{+/+}$ (left) and RTN4RL2$^{-/-}$ (right) cochleae of p21-30 mice. Synapses are visualized by staining against Ctbp2/Ribeye (ribbons) and Homer1 (PSDs). Scale bar = 5 µm. (**B**) The number of the ribbons is not affected along the tonotopic axis in RTN4RL2$^{-/-}$ cochleae. (**C**) The size of the ribbons is increased in IHCs of both apical and middle turns in RTN4RL2$^{-/-}$ cochleae ($p < 0.001$, Mann-Whitney-Wilcoxon test). N = 6 animals/genotype. Box-whisker plots show the median, 25/75 percentiles (box) and the range (whiskers). Individual data points are overlaid.

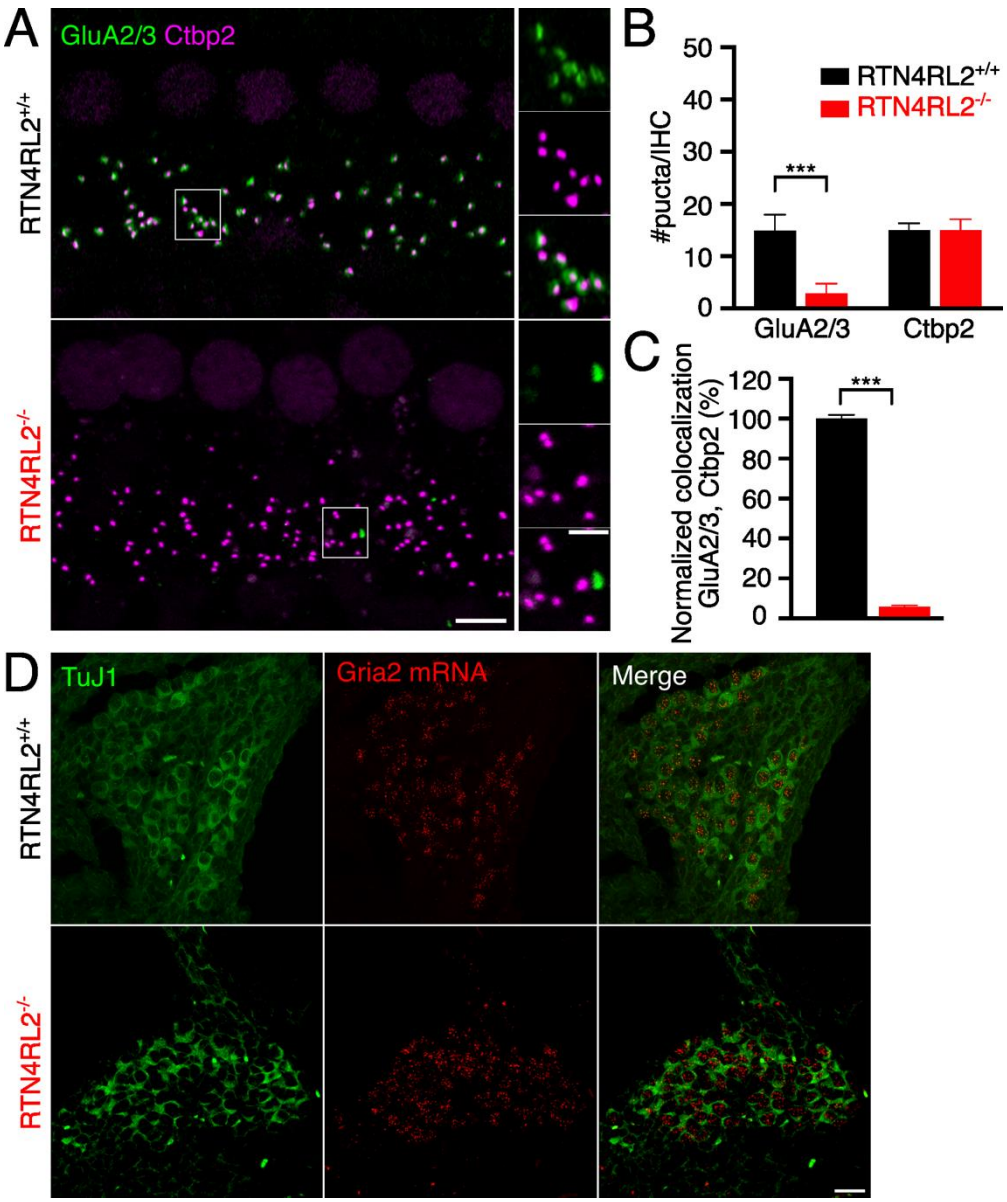

Figure 2-figure supplement 3. Reduced GluA2/3 signal juxtaposing presynaptic ribbons in IHCs of RTN4RL2$^{-/-}$ mice. (**A**) Maximal intensity projections of representative IHC regions from RTN4RL2$^{+/+}$ (top) and RTN4RL2$^{-/-}$ (bottom) cochleae immunolabeled against Ctbp2/Ribeye (ribbons) and GluA2/3 (AMPA receptors of PSD). Scale bar = 5 μm. The zoom-in regions marked with the white rectagles are presented on the right-hand side. Scale bar = 2 μm. (**B**) The number of the GluA2/3 positive puncta is drastically reduced in RTN4RL2$^{-/-}$ mice despite the maintained number of presynaptic ribbons ($p < 0.001$, Mann-Whitney-Wilcoxon test). (**C**) Disrupted colocalization of Ctbp2/Ribeye and GluA2 immunofluorescence puncta at IHCs of RTN4RL2$^{-/-}$ mice ($p < 0.001$, Mann-Whitney-Wilcoxon test). N = 6 animals/genotype. (**D**) Representative images of RNAscope ISH from p4 mice show maintained expression of Gria2 (red dots) in the SGN somata of RTN4RL2$^{-/-}$ mice. Scale bar = 10 μm.

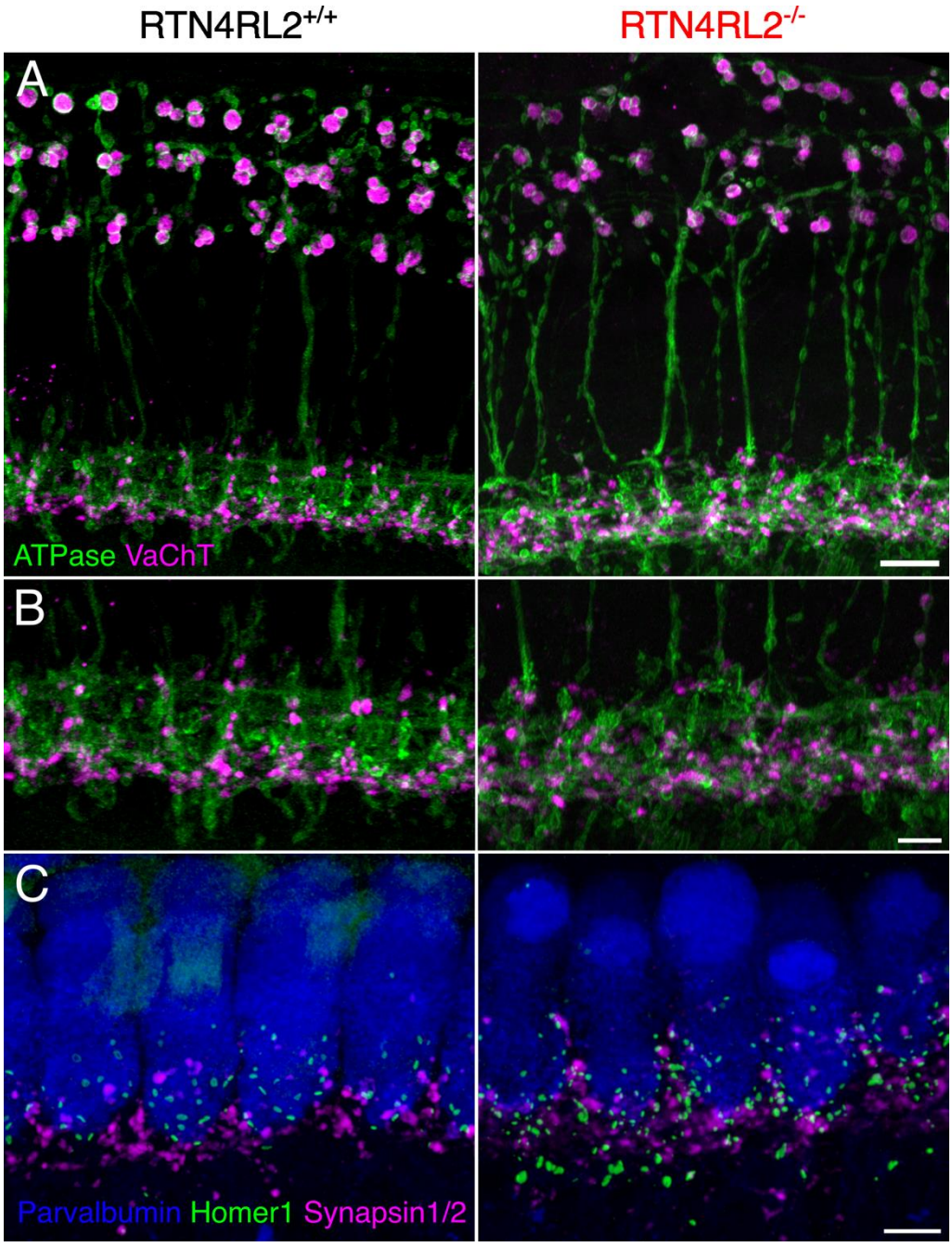

Figure 2-figure supplement 4. Efferent innervation pattern in RTN4RL2$^{-/-}$ cochleae. (**A**) Maximal intensity projections of confocal stacks of outer and inner hair cell regions at the apical region of the cochlea from p21-30 RTN4RL2$^{+/+}$ (left) and RTN4RL2$^{-/-}$ (right) mice. SGN fibers/terminals and efferent terminals are visualized staining for Na^+/K^+ ATPase and vesicular acetylcholine transporter (VaChT), respectively. Scale Bar = 10 µm (**B**) Same as (A) but zoomed into the IHC region. Scale Bar = 5 µm (**C**) Maximal intensity projections of confocal stacks of a row of apical IHC region from p21 RTN4RL2$^{+/+}$ (left) and RTN4RL2$^{-/-}$ (right) mice. Presynaptic efferent terminals were stained with an anti-synapsin1/2 antibody. Scale bar = 5 µm.

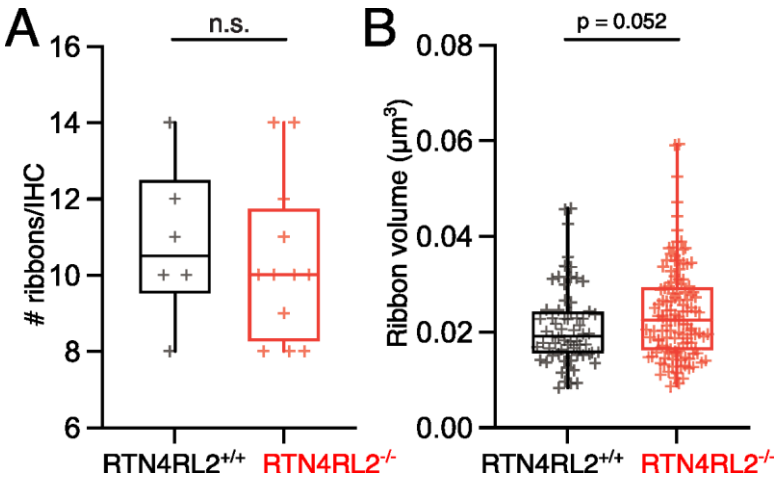

Figure 3-figure supplement 1. Quantification of ribbon number and volume in SBEM reconstructions. (**A**) The number of ribbons is not changed in RTN4RL2$^{-/-}$ IHCs (RTN4RL2$^{-/-}$: 10.3 ± 0.61, SD = 2.1, n = 12, N = 2 vs. RTN4RL2$^{+/+}$: 10.8 ± 0.83, SD = 2.04, n = 6, N = 1; p = 0.54, Mann-Whitney-Wilcoxon test). (**B**) Ribbon volumes tend to be larger in RTN4RL2$^{-/-}$ IHCs without reaching statistical significance (RTN4RL2$^{-/-}$: 0.024 ± 0.001 µm^3, SD = 0.01 µm^3, n = 125 ribbons in 12 IHCs, N = 2 vs. RTN4RL2$^{+/+}$: 0.021 ± 0.001 µm^3, SD = 0.008 µm^3, n = 65 ribbons in 6 IHCs, N = 1; p = 0.06, Mann-Whitney-Wilcoxon test). Box-whisker plots show the median, 25/75 percentiles (box) and the range (whiskers). Individual data points are overlaid.

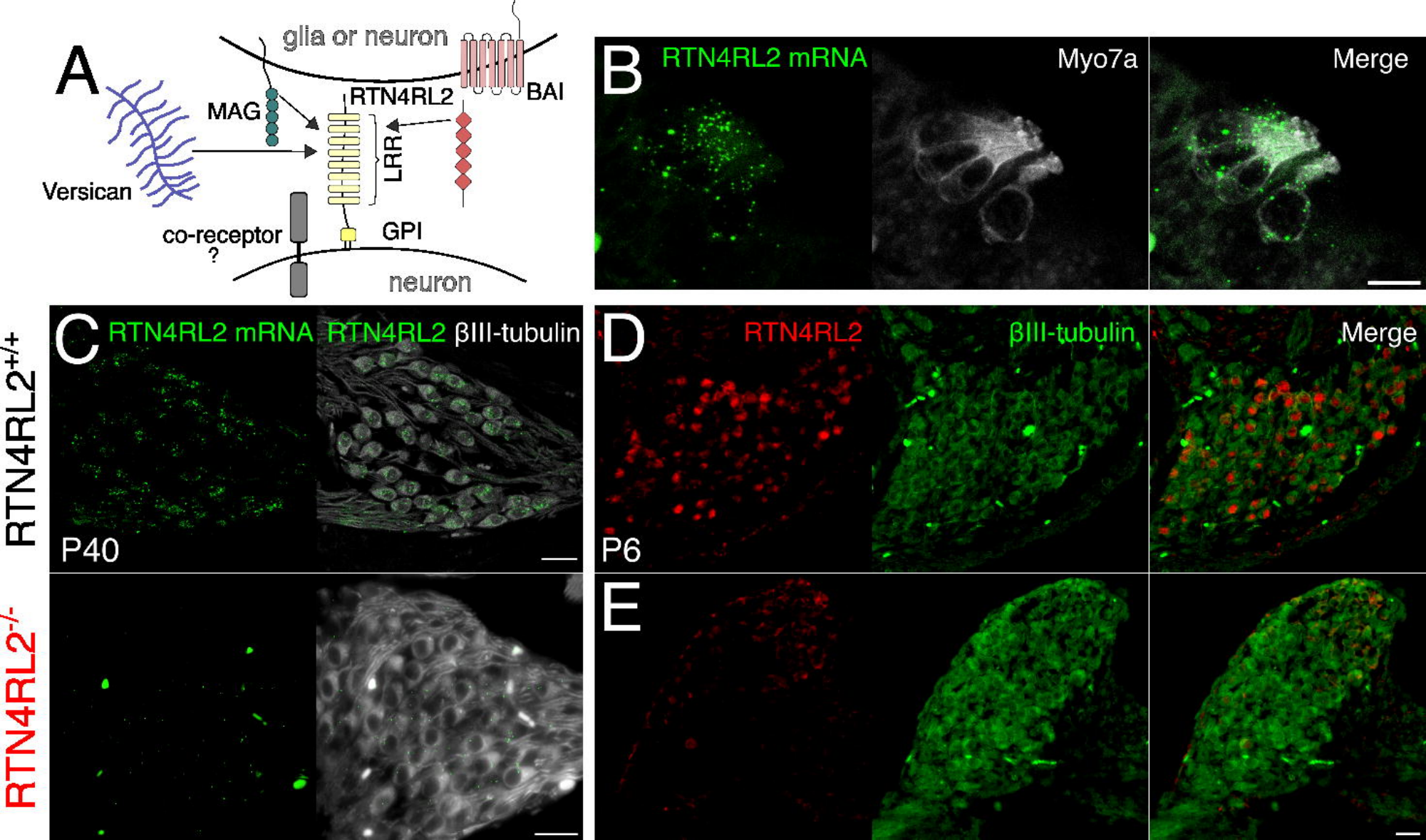
A
glia or neuron
BAI
RTN4RL2
MAG
LRR
Versican
co-receptor
?
GPI
neuron
B
RTN4RL2 mRNA
Myo7a
Merge
C
RTN4RL2 mRNA
RTN4RL2
βIII-tubulin
P40
D
RTN4RL2
βIII-tubulin
Merge
P6
E
RTN4RL2+/+
RTN4RL2-/-

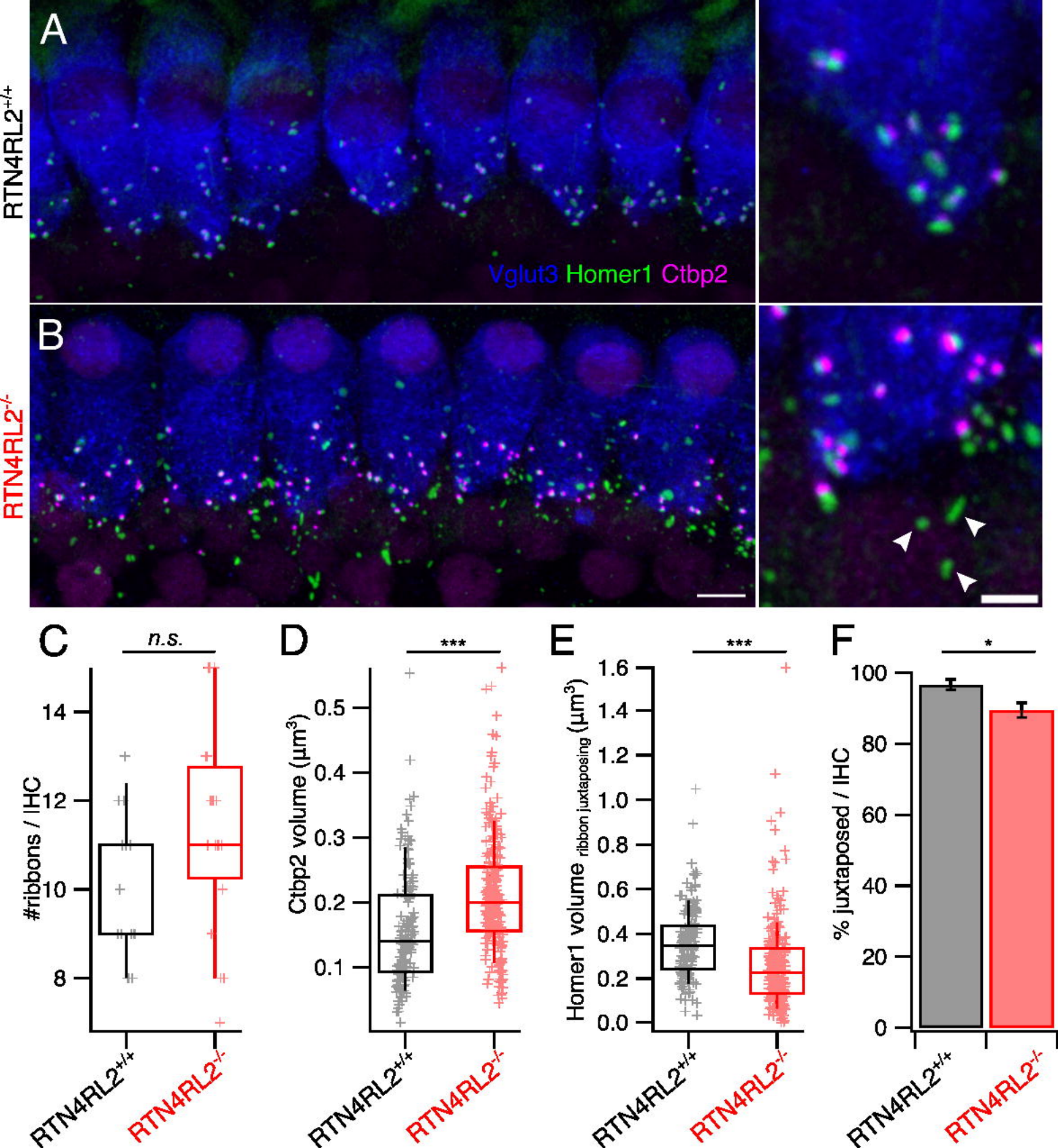
A
RTN4RL2+/+
Vglut3 Homer1 Ctbp2
B
RTN4RL2-/-
C
n.s.
#ribbons / IHC
D
***
Ctbp2 volume (µm3)
E
***
Homer1 volume ribbon juxtaposing (µm3)
F
*
% juxtaposed / IHC
RTN4RL2+/+
RTN4RL2-/-

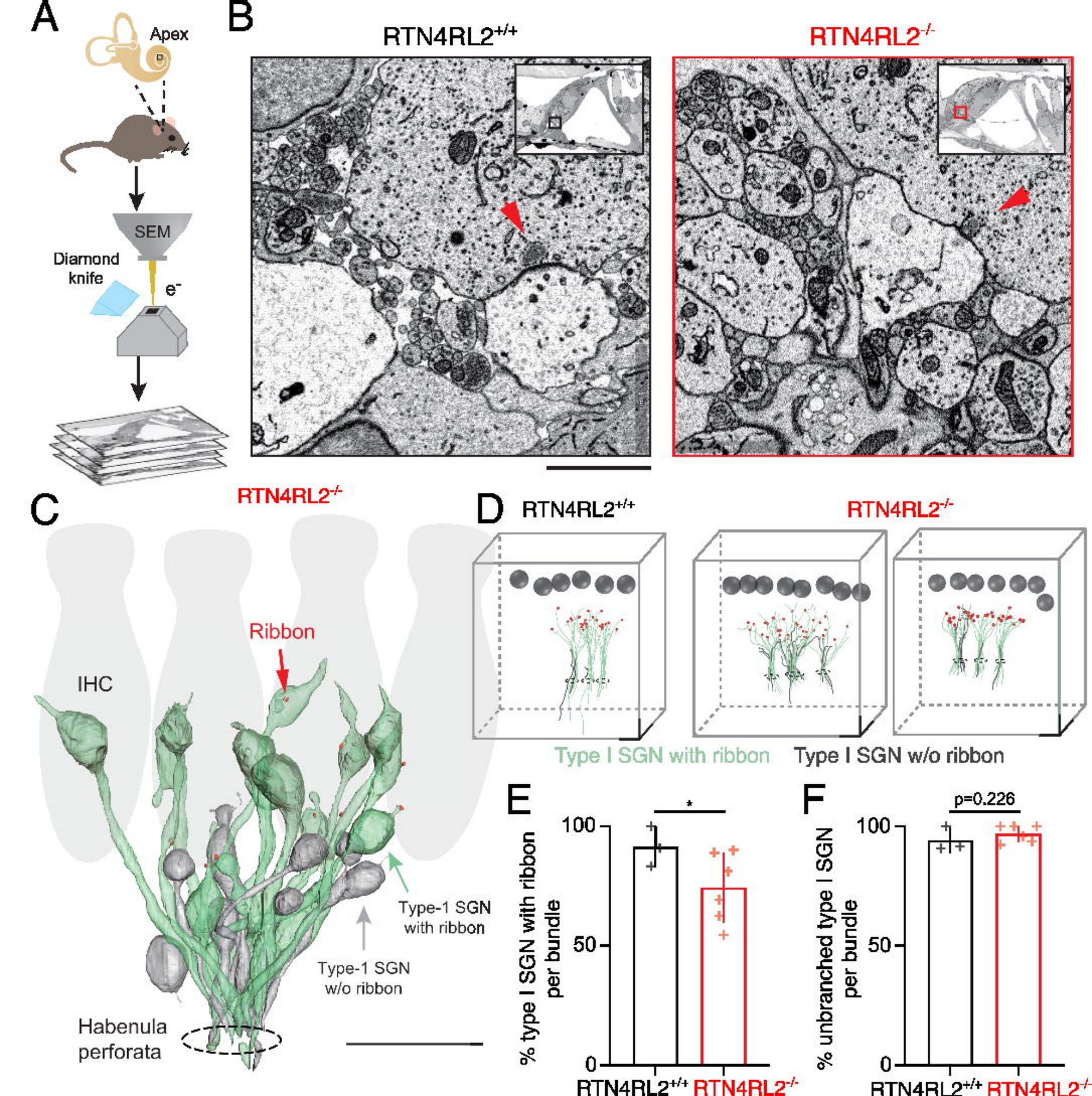
A
Apex
SEM
Diamond knife
e⁻
B
RTN4RL2+/+
RTN4RL2-/-
C
RTN4RL2-/-
Ribbon
IHC
Type-1 SGN with ribbon
Type-1 SGN w/o ribbon
Habenula perforata
D
RTN4RL2+/+
RTN4RL2-/-
Type I SGN with ribbon
Type I SGN w/o ribbon
E
% type I SGN with ribbon per bundle
100
50
0
*
RTN4RL2+/+
RTN4RL2-/-
F
% unbranched type I SGN per bundle
100
50
0
p=0.226
RTN4RL2+/+
RTN4RL2-/-

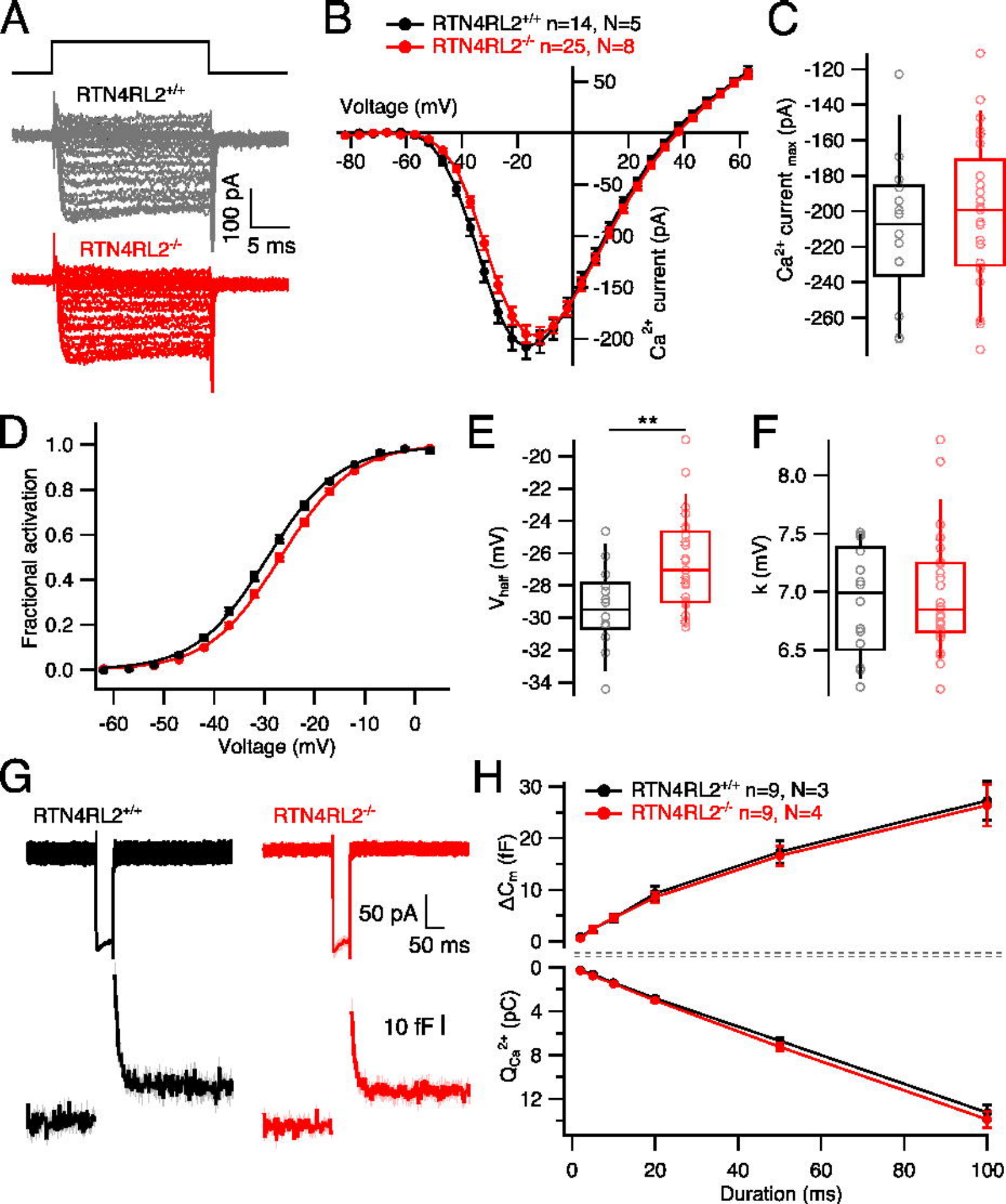
A
RTN4RL2+/+
RTN4RL2-/-
100 pA
5 ms
B
RTN4RL2+/+ n=14, N=5
RTN4RL2-/- n=25, N=8
Voltage (mV)
Ca2+ current (pA)
C
Ca2+ current max (pA)
D
Fractional activation
Voltage (mV)
E
**
Vhalf (mV)
F
k (mV)
G
RTN4RL2+/+
RTN4RL2-/-
50 pA
50 ms
10 fF
H
RTN4RL2+/+ n=9, N=3
RTN4RL2-/- n=9, N=4
ΔCm (fF)
QCa2+ (pC)
Duration (ms)

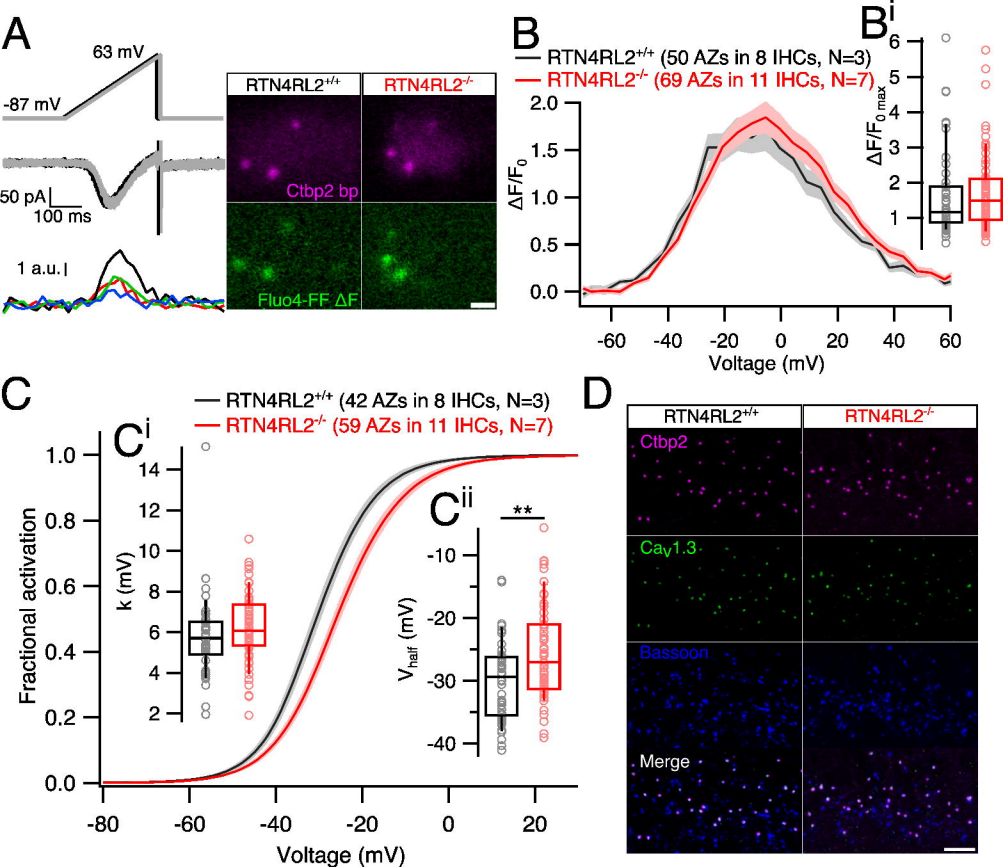
A
63 mV
-87 mV
50 pA
100 ms
1 a.u.
RTN4RL2+/+
RTN4RL2-/-
Ctbp2 bp
Fluo4-FF ΔF
B
RTN4RL2+/+ (50 AZs in 8 IHCs, N=3)
RTN4RL2-/- (69 AZs in 11 IHCs, N=7)
ΔF/F0
Voltage (mV)
Bi
ΔF/F0 max
C
RTN4RL2+/+ (42 AZs in 8 IHCs, N=3)
RTN4RL2-/- (59 AZs in 11 IHCs, N=7)
Fractional activation
Voltage (mV)
Ci
k (mV)
Cii
Vhalf (mV)
**
D
RTN4RL2+/+
RTN4RL2-/-
Ctbp2
CaV1.3
Bassoon
Merge

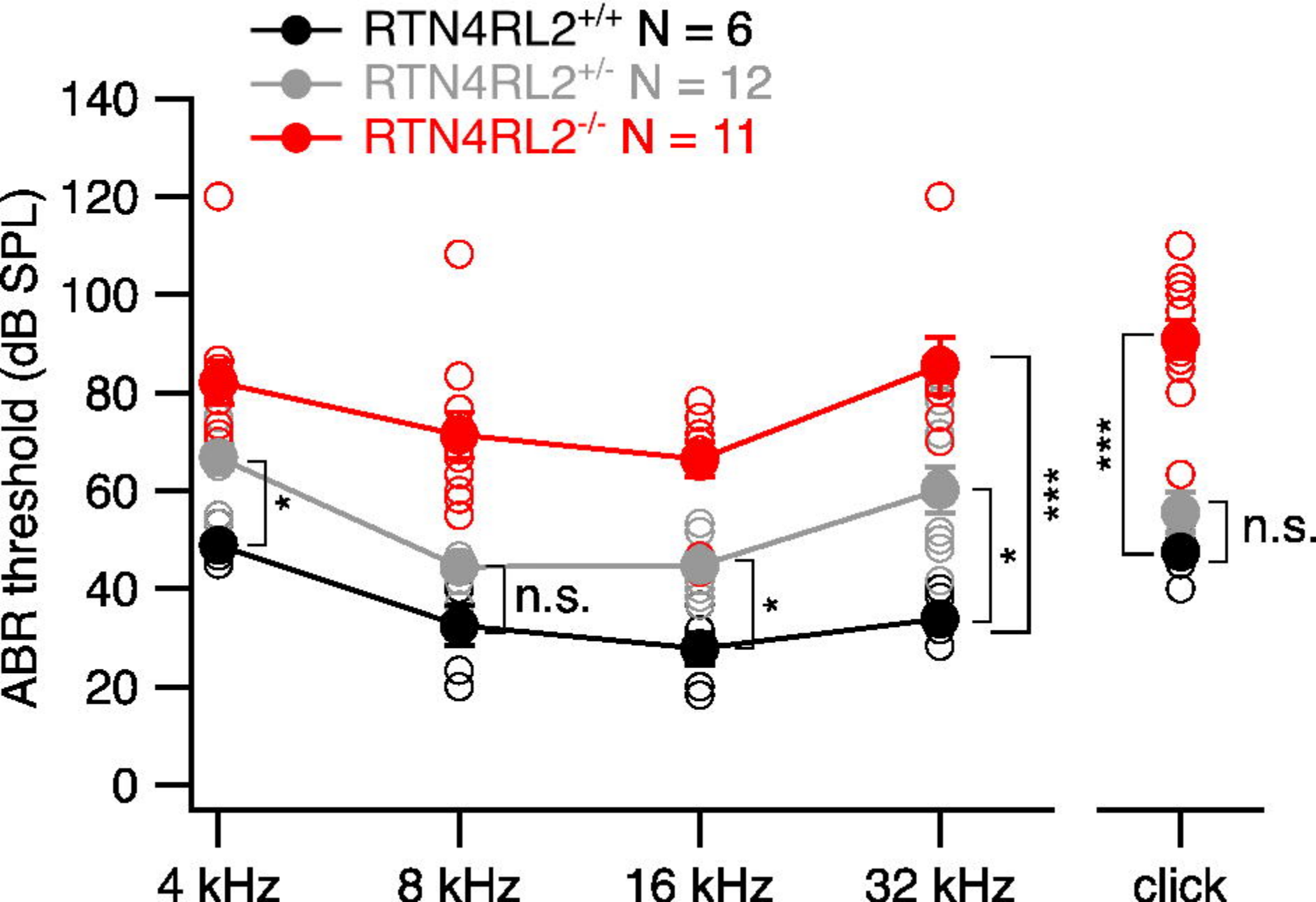
RTN4RL2+/+ N = 6
RTN4RL2+/- N = 12
RTN4RL2-/- N = 11
ABR threshold (dB SPL)
140
120
100
80
60
40
20
0
*
n.s.
*
***
*
***
n.s.
4 kHz
8 kHz
16 kHz
32 kHz
click

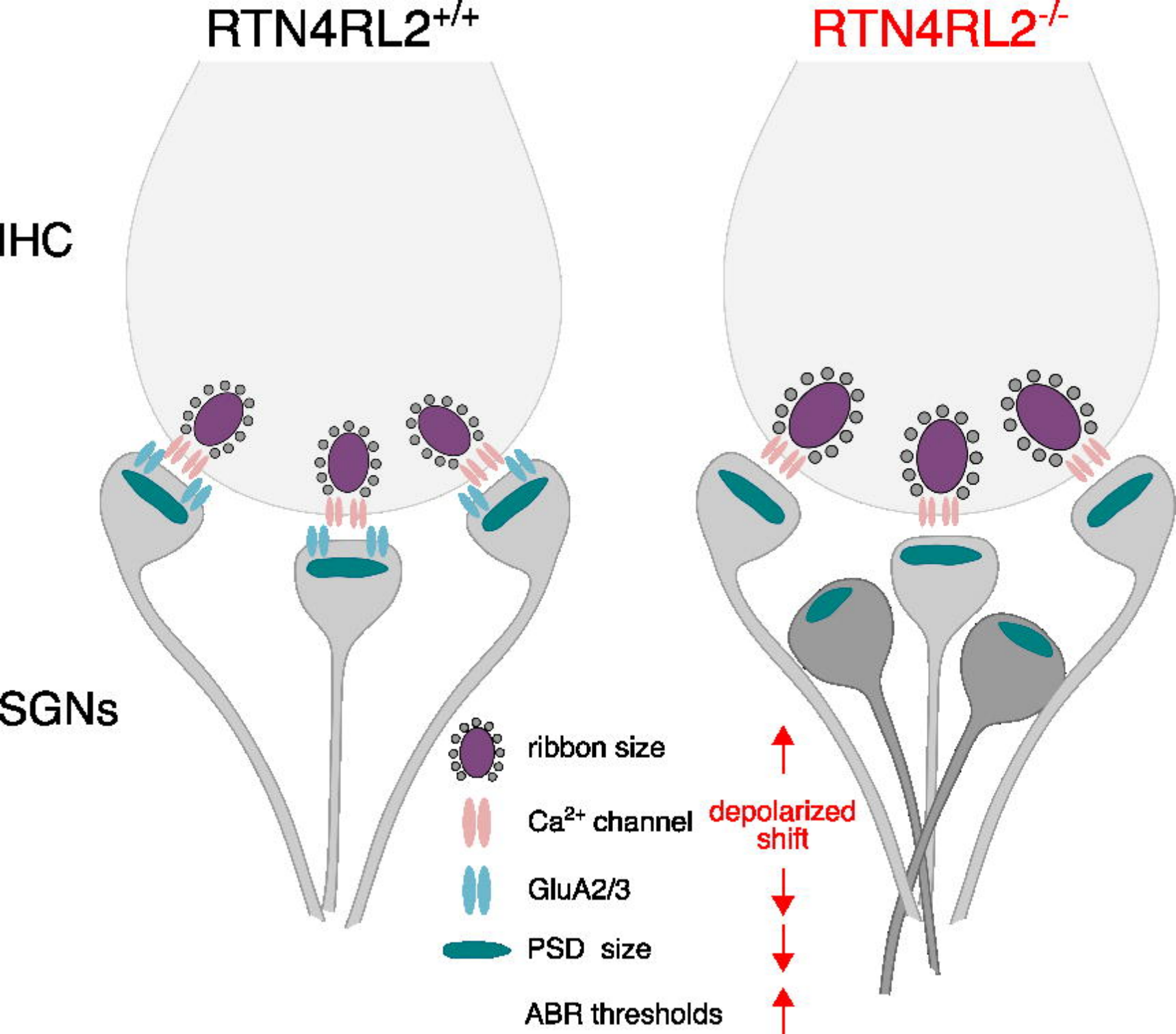
RTN4RL2+/+
RTN4RL2-/-
IHC
SGNs
ribbon size
Ca2+ channel
GluA2/3
PSD size
ABR thresholds
depolarized shift